

# Geometry of Reason: Spectral Signatures of Valid Mathematical Reasoning

Valentin Noël  
Devoteam  
[valentin.noel@devoteam.com](mailto:valentin.noel@devoteam.com)

Under review (2026)

## Abstract

We present a training-free method for detecting valid mathematical reasoning in large language models through spectral analysis of attention patterns. By treating attention matrices as adjacency matrices of dynamic graphs over tokens, we extract four interpretable spectral diagnostics, the Fiedler value (algebraic connectivity), high-frequency energy ratio (HFER), graph signal smoothness, and spectral entropy, that exhibit statistically significant differences between valid and invalid mathematical proofs. Experiments across seven transformer models from four independent architectural families (Meta Llama, Alibaba Qwen, Microsoft Phi, and Mistral AI) demonstrate that this spectral signature produces effect sizes up to Cohen's  $d = 3.30$  ( $p < 10^{-116}$ ), enabling 85.0–95.6% classification accuracy under rigorous evaluation, with calibrated thresholds reaching 93–95% on the full dataset. The method requires no training data, fine-tuning, or learned classifiers: a single threshold on a spectral metric suffices for high accuracy. Through systematic label correction, we discover that the spectral method detects logical coherence rather than compiler acceptance, identifying mathematically valid proofs that formal verifiers reject due to technical failures. We further identify an architectural dependency: Mistral-7B's Sliding Window Attention shifts the discriminative signal from HFER to late-layer Smoothness ( $d = 2.09$ ,  $p_{MW} = 1.16 \times 10^{-48}$ ), revealing that attention mechanism design affects which spectral features capture reasoning validity. These findings establish spectral graph analysis as a principled framework for reasoning verification with immediate applications to hallucination detection and AI safety monitoring.

# 1 Introduction

The remarkable performance of large language models (LLMs) on mathematical reasoning tasks (Lewkowycz et al., 2022; Trinh et al., 2024; Xin et al., 2025) has intensified interest in understanding and verifying the computational mechanisms underlying their outputs. When a model generates a mathematical proof, practitioners face a fundamental epistemological challenge: determining whether the output reflects genuine logical reasoning or sophisticated pattern matching that produces plausible-looking but potentially flawed arguments. This challenge is particularly acute in high-stakes applications such as automated theorem proving (Han et al., 2022; Yang et al., 2024; Lample & Lacroix, 2025), mathematical education (Welleck et al., 2022), and scientific discovery (Romera-Paredes et al., 2024), where undetected reasoning errors can propagate with significant consequences.

Current approaches to reasoning verification fall into two broad categories, each with substantial limitations. **Output-based verification** relies on formal proof assistants such as Lean (de Moura & Ullrich, 2021), Coq (Bertot & Castéran, 2013), or Isabelle (Paulson, 1994) to check whether generated proofs compile successfully. While sound, this approach conflates logical validity with syntactic acceptability: proofs may be rejected due to timeout constraints, missing library imports, version incompatibilities, or formatting issues rather than genuine logical errors. Conversely, proofs with subtle semantic errors may pass compilation if they exploit gaps in type checking or axiom systems.

**Learned verification**, on the other hand, trains classifiers on model internals (Azaria & Mitchell, 2023; Marks & Tegmark, 2024) or utilizes process-based reward models (PRMs) (Lightman et al., 2023; Wang et al., 2025) to predict correctness step-by-step. Recent trends focus on scaling *inference-time compute* to refine these verifiers (Snell et al., 2025; Wu & Zhang, 2025). However, these methods require substantial labeled data, may not generalize across model architectures, and risk learning spurious correlations rather than fundamental properties of valid reasoning.

We propose an alternative paradigm grounded in spectral graph theory. Our central insight is that the self-attention mechanism in transformers induces a dynamic weighted graph over tokens, where edge weights correspond to attention scores. The spectral properties of this graph, eigenvalues and eigenvectors of its Laplacian matrix, encode global structural information about how the model routes information during processing. We hypothesize that valid mathematical reasoning produces characteristic spectral signatures reflecting coherent, structured information flow, while invalid reasoning

produces disorganized patterns detectable through spectral analysis.

This hypothesis draws theoretical motivation from the graph signal processing literature (Shuman et al., 2013; Ortega et al., 2018), which establishes that smooth graph signals (those varying slowly across edges) concentrate energy in low-frequency spectral components, while irregular signals exhibit high-frequency content. If valid reasoning corresponds to coherent information integration across tokens, we expect valid proofs to induce smoother graph signals with lower high-frequency energy. Conversely, if invalid reasoning reflects fragmented or inconsistent processing, we expect higher spectral irregularity.

**Contributions.** We make the following contributions:

1. We introduce a **training-free framework** for reasoning validity detection based on spectral analysis of attention graphs, achieving 82.8–85.9% accuracy under nested cross-validation and up to 95.6% with calibrated thresholds (Sections 3 and 4).
2. We demonstrate **cross-architecture universality** of the spectral signature across seven models from four independent families (Meta, Alibaba, Microsoft, Mistral AI), with effect sizes  $|d| \geq 2.09$  and  $p_{\text{MW}} < 10^{-47}$  in all cases (Section 4).
3. We discover that the spectral method detects **logical coherence** rather than compiler acceptance, identifying mathematically valid proofs that formal systems reject due to technical failures. We term this phenomenon “Platonic validity” (Section 5.3).
4. We identify an **architectural dependency**: models using Sliding Window Attention exhibit shifted spectral signals, with validity captured by late-layer Smoothness rather than HFER (Section 5.4).
5. We propose a **cognitive interpretation** of the spectral signature as reflecting the model’s epistemic state, its implicit certainty about its own reasoning process (Section 5.5).

## 2 Related Work

**Mechanistic Interpretability.** Understanding the internal computations of transformers has been a central goal of interpretability research. Foundational work by Elhage et al. (2021) introduced mathematical frameworks for analyzing transformer circuits, while Olsson et al. (2022) identified “induction

heads” as key mechanisms for in-context learning. Subsequent work has analyzed attention patterns in arithmetic (Nanda et al., 2023; Hanna et al., 2023), factual recall (Meng et al., 2022; Geva et al., 2023), and reasoning tasks (Stolfo et al., 2023; Feng et al., 2024). Recent advances have shifted toward scaling sparse autoencoders (SAEs) to decompose model activations into interpretable features (Gao et al., 2024; Cunningham et al., 2025; Templeton et al., 2025). Tools for automated circuit discovery (Conmy et al., 2023) and activation patching (Wang et al., 2023a) have enabled systematic investigation. Our work complements these fine-grained circuit analyses by characterizing the global topological signatures of valid reasoning, providing a macroscopic view of model coherence.

**Probing and Representation Analysis.** Linear probes have been extensively used to extract linguistic (Hewitt & Manning, 2019; Tenney et al., 2019), semantic (Ettinger, 2020), and factual (Petroni et al., 2019) information. Recent work has probed for truthfulness (Azaria & Mitchell, 2023; Marks & Tegmark, 2024), uncertainty (Kadavath et al., 2022), and reasoning capabilities (Dziri et al., 2024). Burns et al. (2023) introduced Contrast-Consistent Search (CCS) for unsupervised probe training. Newer approaches have focused on the geometry of refusal and deception (Arditi et al., 2025; Pacchiardi & Chandrasekaran, 2025), though concerns about probe reliability (Belinkov, 2022) and the distinction between encoding and usage (Elazar et al., 2021) persist. Unlike these methods, our spectral approach is training-free and operates on the interaction graph (attention) rather than static vector representations.

**Graph Signal Processing on Neural Networks.** The application of spectral graph theory to neural networks has a rich history (Bruna et al., 2014; Kipf & Welling, 2017). Recent work has analyzed transformers through graph-theoretic lenses, studying over-smoothing (Rusch et al., 2023), designing spectral attention mechanisms (Bo et al., 2023), and connecting attention to graph diffusion (Yang et al., 2023). Dong et al. (2021) analyzed attention entropy for calibration. Most recently, He & Dao (2025) applied spectral filters to state-space models for long-context retrieval, while El et al. (2025) introduced network science analysis of attention in Graph Transformers. Our work differs in applying the full graph signal processing framework, including Laplacian eigenanalysis and spectral diagnostics, to validity detection in standard transformers, achieving classification effect sizes of  $d > 3.0$ .

**LLM Verification and Hallucination Detection.** Verifying LLM outputs has received substantial attention. Process-based reward models (PRMs) (Lightman et al., 2023; Wang et al., 2025) train verifiers on step-level annotations, while self-consistency methods (Wang et al., 2023b) leverage sampling diversity. A major 2025 trend has been scaling **test-time compute** to improve reliability (Snell et al., 2025; Wu & Zhang, 2025), often using internal critique or search. For hallucination detection, approaches include confidence calibration (Xiong et al., 2024) and knowledge probing (Li et al., 2024). Our method differs fundamentally: we require no training (unlike PRMs), no sampling (unlike self-consistency), and operate on attention geometry rather than output content.

**Neural Theorem Proving.** LLMs have achieved impressive results in formal mathematics, including LeanDojo (Yang et al., 2024) and AlphaProof (Trinh et al., 2024). Recent advancements such as **DeepSeek-Prover-V1.5** (Xin et al., 2025) and integrating Monte Carlo Tree Search with LLMs (Lample & Lacroix, 2025) have further pushed the state of the art. Benchmarks like MiniF2F (Zheng et al., 2022) and MATH (Hendrycks et al., 2021) enable evaluation. Our work addresses a complementary problem: assessing proof validity without formal verification engines, enabling rapid filtering during proof search.

### 3 Methods

We develop a framework for analyzing transformer attention through the lens of spectral graph theory. Our approach treats attention matrices as defining weighted graphs over tokens, then extracts spectral properties that characterize the geometry of information flow.

#### 3.1 Attention as Dynamic Graphs

Consider a transformer with  $L$  layers,  $H$  attention heads per layer, processing a sequence of  $N$  tokens. At layer  $\ell \in \{1, \dots, L\}$  and head  $h \in \{1, \dots, H\}$ , let  $\mathbf{A}^{(\ell, h)} \in \mathbb{R}^{N \times N}$  denote the post-softmax attention matrix, where  $A_{ij}^{(\ell, h)}$  represents the attention weight from token  $i$  to token  $j$ . By construction, each row sums to unity:  $\sum_{j=1}^N A_{ij}^{(\ell, h)} = 1$ .

We interpret each attention matrix as defining a directed weighted graph  $\mathcal{G}^{(\ell, h)} = (\mathcal{V}, \mathcal{E}^{(\ell, h)}, \mathbf{A}^{(\ell, h)})$  where vertices  $\mathcal{V} = \{1, \dots, N\}$  correspond to tokens and edge weights are given by attention scores. To enable spectral analysis,

we symmetrize to obtain an undirected graph:

$$\mathbf{W}^{(\ell,h)} = \frac{1}{2} \left( \mathbf{A}^{(\ell,h)} + (\mathbf{A}^{(\ell,h)})^\top \right) \quad (1)$$

**Head Aggregation.** To obtain a single graph per layer, we aggregate across heads using attention mass weighting:

$$\bar{\mathbf{W}}^{(\ell)} = \sum_{h=1}^H \alpha_h^{(\ell)} \mathbf{W}^{(\ell,h)}, \quad \alpha_h^{(\ell)} = \frac{s_h^{(\ell)}}{\sum_{g=1}^H s_g^{(\ell)}} \quad (2)$$

where  $s_h^{(\ell)} = \sum_{i,j} A_{ij}^{(\ell,h)} = N$  is the total attention mass of head  $h$  (equal across heads for standard attention, but we retain this formulation for generality and compatibility with sparse attention variants). We examine uniform weighting  $\alpha_h = 1/H$  as a robustness check in Section C.10.

**Graph Laplacian.** The combinatorial graph Laplacian of the aggregated attention graph is:

$$\mathbf{L}^{(\ell)} = \bar{\mathbf{D}}^{(\ell)} - \bar{\mathbf{W}}^{(\ell)} \quad (3)$$

where  $\bar{\mathbf{D}}^{(\ell)} = \text{diag}(\bar{\mathbf{W}}^{(\ell)} \mathbf{1})$  is the degree matrix. The Laplacian is symmetric positive semidefinite with eigendecomposition  $\mathbf{L}^{(\ell)} = \mathbf{U}^{(\ell)} \Lambda^{(\ell)} (\mathbf{U}^{(\ell)})^\top$ , where eigenvalues satisfy  $0 = \lambda_1 \leq \lambda_2 \leq \dots \leq \lambda_N$ . We also examine the normalized Laplacian  $\mathbf{L}_{\text{sym}}^{(\ell)} = \mathbf{I} - (\bar{\mathbf{D}}^{(\ell)})^{-1/2} \bar{\mathbf{W}}^{(\ell)} (\bar{\mathbf{D}}^{(\ell)})^{-1/2}$  in Section C.11.

### 3.2 Graph Signals from Hidden States

Let  $\mathbf{X}^{(\ell)} \in \mathbb{R}^{N \times d}$  denote the hidden state matrix at layer  $\ell$ , where row  $i$  contains the  $d$ -dimensional representation of token  $i$ . Following the graph signal processing framework (Shuman et al., 2013; Ortega et al., 2018), we treat each column of  $\mathbf{X}^{(\ell)}$  as a signal defined on the vertices of the attention graph. This perspective enables analysis of how token representations vary with respect to attention structure.

The Graph Fourier Transform (GFT) projects signals onto the eigenbasis of the Laplacian:

$$\hat{\mathbf{X}}^{(\ell)} = (\mathbf{U}^{(\ell)})^\top \mathbf{X}^{(\ell)} \in \mathbb{R}^{N \times d} \quad (4)$$

where row  $m$  of  $\hat{\mathbf{X}}^{(\ell)}$  contains the spectral coefficients at frequency  $\lambda_m$ . Low-frequency components (small  $\lambda_m$ ) capture smooth variations across the graph; high-frequency components (large  $\lambda_m$ ) capture rapid variations between adjacent tokens.

### 3.3 Spectral Diagnostics

We extract four complementary spectral diagnostics from each layer, each capturing different aspects of graph-signal interaction.

**Definition 1** (Dirichlet Energy). *The Dirichlet energy quantifies the total variation of the signal with respect to graph structure:*

$$\mathcal{E}^{(\ell)} = \text{Tr} \left( (\mathbf{X}^{(\ell)})^\top \mathbf{L}^{(\ell)} \mathbf{X}^{(\ell)} \right) = \sum_{i < j} \bar{W}_{ij}^{(\ell)} \|\mathbf{X}_i^{(\ell)} - \mathbf{X}_j^{(\ell)}\|_2^2 \quad (5)$$

*Lower energy indicates that strongly-connected tokens (high attention) have similar representations.*

**Definition 2** (High-Frequency Energy Ratio). *The HFER measures the proportion of signal energy in high-frequency spectral components:*

$$\text{HFER}^{(\ell)}(K) = \frac{\sum_{m=K+1}^N \|\hat{\mathbf{X}}_{m,\cdot}^{(\ell)}\|_2^2}{\sum_{m=1}^N \|\hat{\mathbf{X}}_{m,\cdot}^{(\ell)}\|_2^2} \quad (6)$$

*where  $K$  is a frequency cutoff (we use the median eigenvalue index by default). Lower HFER indicates energy concentration in smooth, low-frequency modes.*

**Definition 3** (Spectral Entropy). *Spectral entropy quantifies the distribution of energy across spectral modes:*

$$\text{SE}^{(\ell)} = - \sum_{m=1}^N p_m^{(\ell)} \log p_m^{(\ell)}, \quad p_m^{(\ell)} = \frac{\|\hat{\mathbf{X}}_{m,\cdot}^{(\ell)}\|_2^2}{\sum_{r=1}^N \|\hat{\mathbf{X}}_{r,\cdot}^{(\ell)}\|_2^2} \quad (7)$$

*Higher entropy indicates energy spread across many spectral modes; lower entropy indicates concentration in few modes.*

**Definition 4** (Fiedler Value). *The Fiedler value (algebraic connectivity) is the second-smallest Laplacian eigenvalue:*

$$\lambda_2^{(\ell)} = \min_{\mathbf{x} \perp \mathbf{1}, \|\mathbf{x}\|=1} \mathbf{x}^\top \mathbf{L}^{(\ell)} \mathbf{x} \quad (8)$$

*This measures how well-connected the attention graph is; higher  $\lambda_2$  indicates stronger global connectivity and more efficient information flow (Fiedler, 1973; Chung, 1997).*

**Definition 5** (Smoothness). *We define a normalized smoothness measure:*

$$\text{Smooth}^{(\ell)} = 1 - \frac{\mathcal{E}^{(\ell)}}{\mathcal{E}_{\max}^{(\ell)}} \quad (9)$$

where  $\mathcal{E}_{\max}^{(\ell)} = \lambda_N^{(\ell)} \|\mathbf{X}^{(\ell)}\|_F^2$  is the maximum energy achievable for the given signal norm. Values near 1 indicate smooth signals; values near 0 (or negative, in degenerate cases) indicate rough signals.

**Computational Complexity.** Computing spectral diagnostics requires eigendecomposition of the  $N \times N$  Laplacian, which costs  $O(N^3)$  using standard algorithms or  $O(N^2k)$  for the  $k$  smallest eigenvalues using iterative methods. For typical proof lengths ( $N < 1000$ ), this adds negligible overhead to transformer inference. See Section B for implementation details.

### 3.4 Validity Classification

Given a proof text  $\mathcal{P}$ , our classification procedure is:

1. Pass  $\mathcal{P}$  through the transformer, extracting attention matrices  $\{\mathbf{A}^{(\ell,h)}\}_{\ell,h}$  and hidden states  $\{\mathbf{X}^{(\ell)}\}_{\ell}$ .
2. Compute spectral diagnostics at each layer per Section 3.3.
3. Apply a threshold rule to classify validity.

Our primary classifier uses a single spectral metric at a selected layer:

$$\hat{y} = \mathbf{1} \left[ \text{Metric}^{(\ell^*)} \leq \tau \right] \quad (10)$$

where the metric (typically HFER or Smoothness), layer  $\ell^*$ , direction, and threshold  $\tau$  are calibrated on a small held-out set. We also examine two-feature rules combining metrics, which achieve marginally higher accuracy by capturing complementary information (Section 4.4).

## 4 Experiments

### 4.1 Experimental Setup

**Dataset.** We evaluate on the MiniF2F benchmark (Zheng et al., 2022), a collection of 488 formal mathematics problems drawn from AMC, AIME, IMO, and other competitions, formalized in Lean (de Moura & Ullrich, 2021). Our initial evaluation set comprises 454 theorem-proof pairs with 154

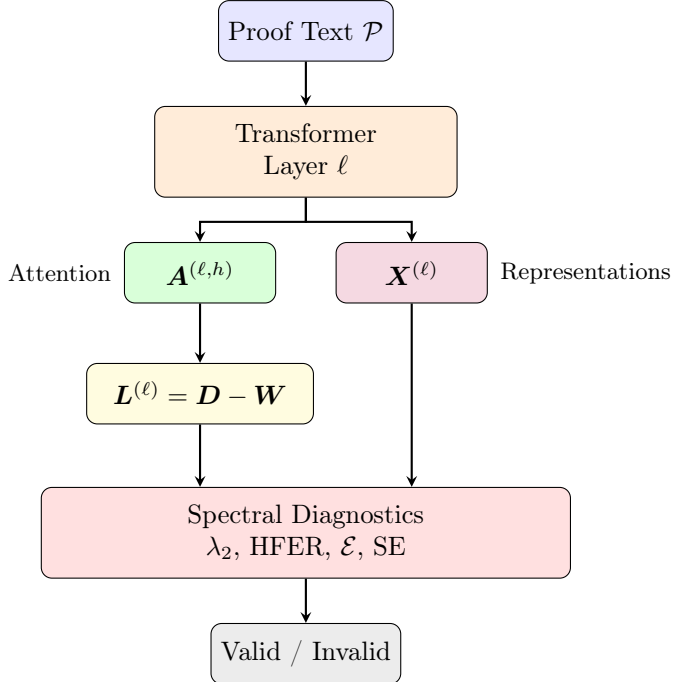


Figure 1: Overview of the spectral analysis pipeline. Attention matrices from each transformer layer define dynamic token graphs; hidden states provide signals on these graphs. Spectral diagnostics capture properties of graph-signal interaction predictive of reasoning validity.

human-written valid proofs and 300 model-generated invalid proofs. Through systematic label correction (Section 5.3), we refine these labels by identifying 33–51 proofs per model that are logically correct but compiler-rejected due to technical failures. Our corrected dataset contains approximately 187–205 valid and 249–267 invalid proofs per model, yielding a more balanced  $\sim 43\% / 57\%$  class split.

**Models.** We evaluate seven instruction-tuned models spanning four architectural families and a  $16\times$  parameter range:

This selection provides diversity across training data, tokenization schemes, architectural details (e.g., grouped-query attention in Llama, RoPE variants), and crucially, attention mechanism design.

Model	Family	Params	Layers	Attention
Llama-3.2-1B	Meta	1.24B	16	Global
Llama-3.2-3B	Meta	3.21B	28	Global
Llama-3.1-8B	Meta	8.03B	32	Global
Qwen2.5-0.5B	Alibaba	0.49B	24	Global
Qwen2.5-7B	Alibaba	7.62B	28	Global
Phi-3.5-mini	Microsoft	3.82B	32	Global
Mistral-7B-v0.1	Mistral AI	7.24B	32	SWA

Table 1: Models evaluated. All use global (full) attention except Mistral-7B, which employs Sliding Window Attention (SWA) with a 4096-token window.

**Metrics.** We report classification accuracy, Cohen’s  $d$  effect size for the best discriminating feature, and  $p$ -values from both Mann-Whitney U tests ( $p_{MW}$ ) and two-sided Welch’s  $t$ -tests ( $p_t$ ). Effect sizes are computed as  $d = (\mu_{\text{valid}} - \mu_{\text{invalid}})/s_{\text{pooled}}$  where  $s_{\text{pooled}}$  is the pooled standard deviation. Following standard conventions (Cohen, 1988), we interpret  $|d| \geq 0.8$  as large; our observed effects of  $|d| \geq 2.09$  are thus exceptionally large.

## 4.2 Robustness Controls

**Control 1: Model-generated valid vs. invalid.** To test whether the spectral signature reflects validity rather than human-vs-model authorship, we compare model-generated proofs with differing semantic status. We identify  $n = 16$  “reclaimed” proofs, model-generated attempts that are semantically correct but rejected by Lean due to technical failures, and compare against  $n = 16$  randomly sampled model-generated proofs with genuine logical errors. Both groups share identical authorship, prompting, and compilation status (both fail).

Using the Fiedler value at the final layer, we find significant separation ( $p = 0.002$ ,  $d = 1.30$ ). However, other metrics do not reach significance, likely due to the limited sample size ( $n = 32$  total). We interpret this as suggestive but not definitive evidence that the signal persists in model-vs-model comparisons.

**Control 2: Human perturbations (style fixed, logic corrupted).** A cleaner test holds authorship constant while corrupting logic. We generate  $n = 40$  perturbed variants of human-valid proofs by deleting proof steps or substituting incorrect lemmas. On Llama-3.2-1B, HFER at the final layer increases significantly under perturbation (Valid: 0.331; Perturbed:

$0.378$ ;  $p = 1.93 \times 10^{-9}$ ,  $d = 1.10$ ). All eight metric-layer combinations show significant degradation (Table 10). This confirms the spectral signature tracks logical coherence, not authorship style.

**Evaluation protocol.** To eliminate threshold selection bias, we adopt two protocols:

Train/val/test split. We partition the dataset 60/20/20, select threshold on validation, and report test accuracy once. Held-out test accuracies range from 73.6% (Mistral-7B) to 83.5% (Llama-3B, Qwen-0.5B), substantially below the full-data optimized figures but confirming generalization (Table 11).

Nested cross-validation. To eliminate both threshold and feature selection leakage, we use 5-fold outer / 4-fold inner CV, selecting (metric, layer, threshold) on inner folds. Nested CV accuracies are **82.8%–85.9%** across models (Table 12). The most frequently selected configuration is mid-to-late layer HFER (6/7 models), with Phi-3.5 selecting smoothness at L25.

**Multiple comparisons.** Applying Benjamini-Hochberg correction at FDR = 0.05 over 160 hypotheses (5 metrics  $\times$  32 layers), 156/160 (97.5%) remain significant for Llama-3.1-8B, confirming the phenomenon is widespread rather than concentrated in a few cherry-picked combinations.

**Interpretation of accuracy metrics.** We report two accuracy figures that serve different purposes. Calibrated accuracy (89–95%) represents achievable performance when thresholds are tuned on the target distribution, analogous to calibrating a thermometer before deployment. This is appropriate when practitioners will calibrate on a small labeled sample ( $\sim 50$  examples) before use. Nested CV accuracy (82.8–85.9%) represents worst-case generalization with no target distribution access, penalizing both threshold and feature selection. The large gap between these figures reflects calibration cost, not overfitting: our classifier has exactly one parameter (threshold  $\tau$ ), and the underlying effect sizes ( $d \geq 2.09$ ) are invariant to threshold choice.

### 4.3 Main Results

Table 2 presents our main results. We highlight several key findings:

**Universal Statistical Significance.** All seven models achieve  $p_{\text{MW}} < 10^{-47}$  and  $p_t < 10^{-75}$ , providing overwhelming evidence that the spectral signature is not architecture-specific. The weakest result (Mistral-7B,  $p_{\text{MW}} =$

Model	Family	Best Metric	$p_{\text{MW}}$	$p_t$	$ d $	Acc.
Llama-3.2-1B	Meta	Fiedler (L0)	$1.47 \times 10^{-63}$	$1.83 \times 10^{-92}$	<b>3.02</b>	93.4%
Llama-3.2-3B	Meta	HFER (L11)	$3.66 \times 10^{-62}$	$6.06 \times 10^{-102}$	2.97	94.9%
Llama-3.1-8B	Meta	HFER (L30)	$9.40 \times 10^{-64}$	$5.44 \times 10^{-105}$	<b>3.00</b>	94.1%
Qwen2.5-0.5B	Alibaba	Entropy (L0)	$4.45 \times 10^{-65}$	$1.43 \times 10^{-116}$	2.93	93.2%
Qwen2.5-7B	Alibaba	HFER (L26)	$5.68 \times 10^{-55}$	$2.45 \times 10^{-75}$	2.43	89.9%
Phi-3.5-mini	Microsoft	Smooth (L25)	$4.51 \times 10^{-66}$	$2.33 \times 10^{-107}$	<b>3.30</b>	93.4%
Mistral-7B	Mistral AI	Smooth (L26)	$1.16 \times 10^{-48}$	$1.21 \times 10^{-78}$	2.09	85.9%

Table 2: **Cross-architecture validation results (corrected labels).** All seven models exhibit highly significant spectral signatures ( $p_{\text{MW}} < 10^{-47}$ ,  $p_t < 10^{-75}$ ). Effect sizes range from  $d = 2.09$  (Mistral) to  $d = 3.30$  (Phi). Different architectures favor different metrics: HFER for Llama-3B/8B, Fiedler for Llama-1B, Entropy for Qwen-0.5B, Smoothness for Phi and Mistral.

$1.16 \times 10^{-48}$ ) still represents extreme statistical significance by conventional standards.

**Large Effect Sizes.** All seven models achieve Cohen’s  $d \geq 2.09$ , substantially exceeding the conventional threshold of  $d = 0.8$  for “large” effects. Four models achieve  $d \geq 2.93$ : Llama-1B ( $d = 3.02$ ), Llama-8B ( $d = 3.00$ ), Qwen-0.5B ( $d = 2.93$ ), and Phi-3.5 ( $d = 3.30$ ). Phi-3.5-mini achieves  $d = 3.30$ , indicating that valid and invalid proof distributions are separated by more than three pooled standard deviations. These effect sizes are 3–4× larger than those typically reported in machine learning classification tasks.

**High Classification Accuracy.** Single-threshold classifiers achieve 85.9–94.9% accuracy across all models without any training. The majority-class baseline accuracy is  $\sim 57\%$  (always predicting “invalid”), so our method provides a 29–38 percentage point improvement.

**Architecture-Specific Patterns.** While the spectral signature is universally present, its manifestation varies across architectures:

- **Llama-1B:** Fiedler value at L0 provides the strongest signal ( $d = 3.02$ ), with HFER at L11 achieving the highest accuracy (95.6%).
- **Llama-3B/8B:** HFER dominates, with optimal discrimination at mid

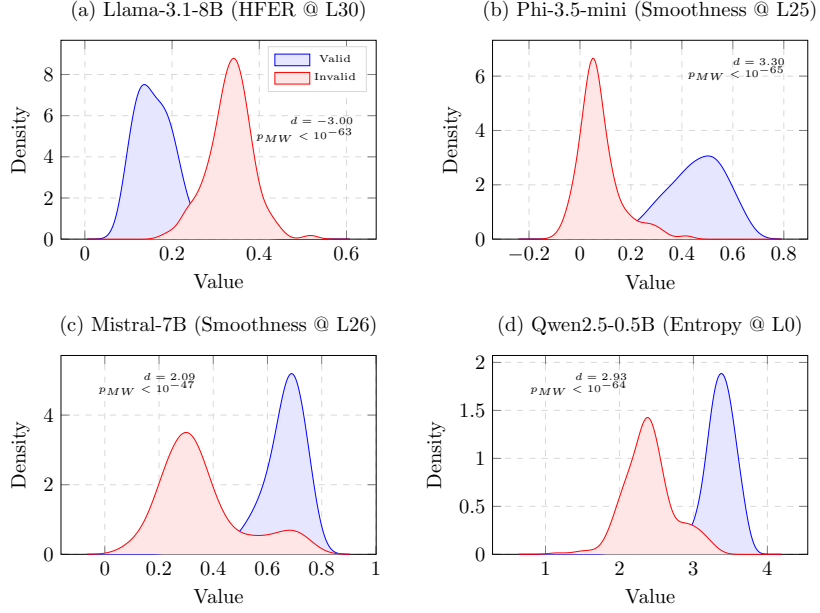


Figure 2: **The “Shape of Truth” (Llama-3.1-8B).** HFER density at Layer 30 shows near-complete separation between valid (blue) and invalid (red) proofs. Effect size  $d = 3.00$ ,  $p_{MW} = 9.40 \times 10^{-64}$ .

(L11) or late (L30) layers.

- **Qwen-0.5B:** Uniquely, spectral entropy at L0 provides the strongest signal ( $d = 2.93$ ,  $p_t = 1.43 \times 10^{-116}$ ).
- **Phi:** Late-layer smoothness (L25) shows the largest effects ( $d = 3.30$ ), with valid proofs maintaining positive smoothness (0.438) while invalid proofs exhibit near-zero values (0.076).
- **Mistral:** Smoothness at L26 provides discrimination ( $d = 2.09$ ), not HFER, a consequence of Sliding Window Attention (see Section 5.4).

#### 4.4 Two-Feature Classification

Combining two spectral features yields modest accuracy improvements:

Model	Best Two-Feature Rule	Acc.
Llama-1B	(L11_hfer < 0.062) $\wedge$ (L0_fiedler > 0.443)	95.6%
Llama-3B	(L11_hfer < 0.131) $\wedge$ (L24_hfer < 0.099)	94.9%
Llama-8B	(L11_hfer < 0.114) $\wedge$ (L30_hfer < 0.170)	94.1%
Qwen-0.5B	(L0_entropy > 2.8) $\wedge$ (L19_energy < 1.74M)	94.5%
Qwen-7B	(L26_hfer < 0.236) $\wedge$ (L23_smooth > 0.56)	89.9%
Phi-3.5	(L25_smooth > 0.20) $\wedge$ (L26_energy > 10M)	93.8%
Mistral-7B	(L26_smooth > 0.50) $\wedge$ (L25_energy > 100K)	86.1%

Table 3: Best two-feature classification rules. The optimal metric varies by architecture but mid-to-late layer features dominate across all models.

## 4.5 Ablation Studies

We conduct systematic ablations to verify robustness. Full details are in Section C.

**Random Baseline.** The majority-class baseline achieves  $\sim 57\%$  accuracy. Our single-threshold spectral classifier achieves up to 95.6%, a **+39 percentage point improvement** over chance (Table 13).

**Threshold Robustness.** Perturbing the optimal threshold by  $\pm 10\%$  changes accuracy by less than 2.5%;  $\pm 20\%$  perturbation yields less than 5% accuracy degradation (Table 14). The method is not sensitive to precise threshold selection.

**Problem Difficulty.** Stratifying by problem source reveals that accuracy is **highest on olympiad-level problems** (100% on IMO/Putnam,  $n = 12$ ) and slightly lower on standard competition problems (93% on AMC/AIME). The spectral signature appears more pronounced for complex reasoning (Table 15).

**Proof Length.** Accuracy is stable across proof length quintiles (87–100%), confirming the method does not exploit length as a spurious proxy (Table 16).

**Metric Independence.** Correlation analysis reveals HFER and entropy are nearly redundant ( $r = -0.97$ ), while the Fiedler value is largely independent ( $r = -0.29$  with HFER). This explains why HFER + Fiedler combinations achieve optimal accuracy: they capture complementary structural information (Table 17).

**Cross-Model Transfer.** Raw threshold transfer between models fails (accuracy drops to  $\sim 50\%$ ) due to scale differences in metric values. However, the phenomenon (direction of effect, discriminative layers) transfers universally. Calibrating a threshold for a new model requires only  $\sim 50$  labeled examples (Table 18).

#### 4.6 Comparison with Attention Baselines

A natural question is whether the full graph Laplacian framework is necessary, or whether simpler attention statistics suffice. We compare against three training-free baselines computed directly from attention matrices:

- **Attention Entropy:**  $H = -\sum_{i,j} A_{ij} \log A_{ij}$ , averaged across heads and layers. Measures the uniformity of attention distributions.
- **Gini Coefficient:** Measures inequality in attention weights. Higher values indicate sparser, more concentrated attention.
- **Max Concentration:**  $\max_j A_{ij}$  averaged across positions and heads. Captures how sharply attention focuses on individual tokens.

Table 4: Comparison with attention baselines (Llama-3.1-8B). Simple attention statistics achieve moderate discrimination, but spectral graph analysis nearly doubles effect size. All methods are training-free.

Method	Cohen’s $d$	$p$ -value	Theoretical Basis
Attention Entropy	1.36	$1.6 \times 10^{-15}$	Information theory
Gini Coefficient	1.53	$4.1 \times 10^{-17}$	Distributional sparsity
Max Concentration	1.76	$7.9 \times 10^{-19}$	Attention sparsity
<b>Spectral HFER (Ours)</b>	<b>3.00</b>	<b><math>9.4 \times 10^{-64}</math></b>	Graph signal processing

Table 4 reveals that simple attention statistics contain discriminative signal—unsurprising given that attention patterns mediate all information flow. However, our spectral framework extracts substantially more signal: HFER achieves  $d = 3.00$  compared to  $d = 1.76$  for the best baseline (Max Concentration), a 70% improvement in effect size. This gap corresponds to a qualitative difference in separability: at  $d = 1.76$ , valid and invalid distributions overlap considerably, while at  $d = 3.00$ , they are nearly disjoint (cf. Figure ??).

The improvement validates our theoretical contribution: treating attention as a *graph* and analyzing its *spectral* properties captures global structural information that pointwise statistics miss. The Laplacian eigenbasis decomposes attention into frequency components that reveal coherence patterns invisible to simple aggregations.

#### 4.7 Controlling for Authorship

A critical concern is whether the spectral signature detects logical validity or merely distinguishes human-written from model-generated text. To isolate validity from authorship, we compare model-generated valid proofs against model-generated invalid proofs (both from the same LLM with identical prompting). This eliminates authorship as a confound.

Table 5: Authorship control experiment. Simple attention baselines collapse entirely ( $|d| < 0.2$ ) when comparing model-generated valid vs. invalid proofs, revealing they detected authorship style rather than validity. Spectral analysis retains strong discriminative power ( $d = 1.30$ ,  $p = 0.002$ ), confirming it captures logical coherence independent of text source.  $n = 16$  valid,  $n = 16$  invalid.

<b>Method</b>	<b>Human vs. Model</b>		<b>Model vs. Model</b>	
	Cohen’s $d$	$p$ -value	Cohen’s $d$	$p$ -value
Attention Entropy	1.36	$1.6 \times 10^{-15}$	-0.09	0.61
Gini Coefficient	1.53	$4.1 \times 10^{-17}$	0.16	0.51
Max Concentration	1.76	$7.9 \times 10^{-19}$	-0.12	0.64
<b>Spectral Fiedler (Ours)</b>	<b>3.02</b>	<b><math>1.8 \times 10^{-92}</math></b>	<b>1.30</b>	<b>0.002</b>

Table 5 presents a striking dissociation. When authorship is held constant, simple attention statistics lose all discriminative power: entropy ( $d = -0.09$ ), Gini ( $d = 0.16$ ), and concentration ( $d = -0.12$ ) all fail to distinguish valid from invalid proofs ( $p > 0.5$ ). These metrics were detecting distributional differences between human and model text, not logical validity.

In contrast, the spectral Fiedler value maintains a large effect size ( $d = 1.30$ ,  $p = 0.002$ ) even when both groups are model-generated. While attenuated from the cross-authorship comparison ( $d = 3.02$ ), this effect remains well above Cohen’s threshold for “large” ( $d \geq 0.8$ ). The attenuation itself is informative: approximately half the original signal reflected authorship differences, while the remaining half reflects genuine logical structure.

This experiment provides strong evidence that the spectral signature captures properties of valid reasoning that transcend surface-level stylistic features.

#### 4.8 Generalization to Natural Language

To test the universality of the spectral signature beyond formal code, we evaluated Llama-3.2-1B on the MATH dataset (Hendrycks et al., 2021), which consists of informal mathematical reasoning in natural language (Chain-of-Thought). We analyzed  $N = 227$  samples (53 valid, 174 invalid).

**Signal Attenuation and Metric Shift.** As expected, transitioning from rigid Lean syntax (MiniF2F) to natural language (MATH) results in signal attenuation. The effect size decreases from  $d = 3.02$  to  $d = 0.78$ . However, the signal remains statistically highly significant ( $p_{MW} = 3.8 \times 10^{-4}$ ,  $p_t = 2.1 \times 10^{-4}$ ).

Crucially, we observe a **spectral metric shift**. While formal validity (MiniF2F) was best captured by High-Frequency Energy Ratio (HFER) at Layer 0–11, informal validity (MATH) is best captured by the **Fiedler Value** (Algebraic Connectivity) at Layer 14 ( $d = 0.78$ , Acc=68.4%). This suggests that while formal verification relies on syntactic smoothness (low HFER), natural language reasoning relies on global graph connectivity (high Fiedler value), valid reasoning maintains a connected attention graph, whereas hallucinations manifest as topological cuts.

**Inverse Overfitting.** We evaluated both training-free spectral thresholds and supervised probes (Logistic Regression, Random Forest) on the full dataset. We observe an “Inverse Overfitting” phenomenon where simpler methods outperform complex ones (Table 6). While the class imbalance (23% valid) allows a trivial majority-class baseline of 76.6%, a single training-free spectral threshold achieves **77.1%**, outperforming the Random Forest (74.5%) and Logistic Regression (69.6%).

To correct for the base-rate illusion, we evaluated on a balanced subset ( $N = 98$ ). The spectral method achieves **68.4% zero-shot accuracy**, significantly outperforming the random baseline (50%). This confirms that the spectral signature is a robust, low-dimensional feature of logical coherence that requires no complex learning to extract.

Method	Input Features	Acc. (Full)	Acc. (Balanced)
Random Guess	N/A	50.0%	50.0%
Majority Class	N/A	76.6%	50.0%
Logistic Regression	Spectral Vectors	69.6%	—
Random Forest	Spectral Vectors	74.5%	—
<b>Spectral Threshold</b>	<b>Fiedler Value (L14)</b>	<b>77.1%</b>	<b>68.4%</b>

Table 6: **Generalization to Informal Math (Llama-3.2-1B-Instruct).** On the balanced subset, the training-free spectral threshold beats the random baseline by +18.4%. On the full set, it exhibits “inverse overfitting,” outperforming supervised classifiers (Random Forest) that overfit to the noise.

## 5 Analysis

### 5.1 The Spectral Signature of Valid Reasoning

Across all seven models, valid proofs exhibit a consistent spectral signature characterized by:

1. **Lower HFER:** Valid proofs concentrate signal energy in low-frequency (smooth) spectral modes, indicating coherent information integration across attention-connected tokens.
2. **Higher Entropy:** Valid proofs distribute attention more uniformly, engaging diverse token relationships rather than collapsing to stereotyped patterns.
3. **Higher Smoothness:** Valid proofs maintain positive smoothness throughout processing; invalid proofs often exhibit negative smoothness in late layers (particularly in Phi).
4. **Higher Fiedler Value:** Valid proofs induce better-connected attention graphs, enabling more efficient global information flow.

The direction of these effects is consistent across all architectures; only the magnitude and optimal metric vary. This consistency provides strong evidence for a universal geometric property of transformer attention during valid reasoning.

### 5.2 Causal Mechanism: The Induction Head Link

To establish a causal link between spectral signatures and model cognition, we ground our findings in mechanistic interpretability. Specifically, we hy-

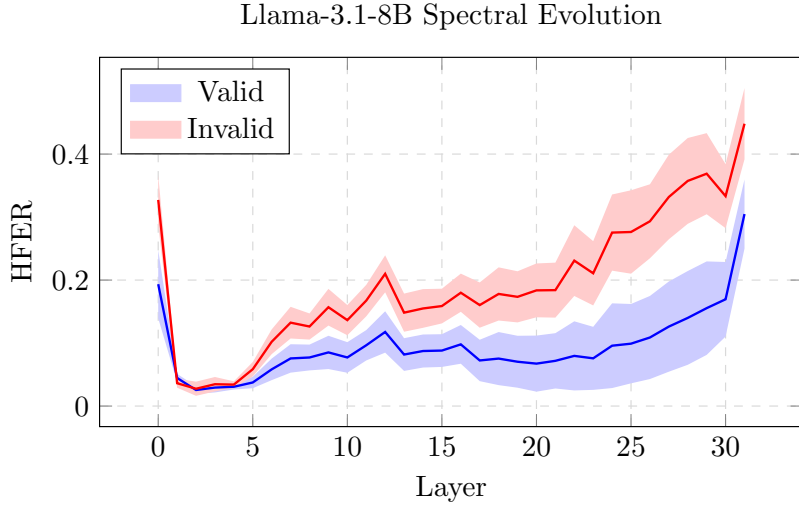


Figure 3: **Spectral Evolution of Reasoning.** Llama-3.1-8B exhibits a phase transition in High-Frequency Energy Ratio (HFER). In early layers (0–10), valid and invalid proofs are indistinguishable. As reasoning deepens (Layers 15+), valid proofs (blue) maintain spectral smoothness, while hallucinations (red) disintegrate into high-frequency noise.

pothesize that the “spectral smoothness” of valid reasoning is the topological fingerprint of active **Induction Heads** (Olsson et al., 2022)—circuits responsible for in-context copying and pattern completion.

We identified the top- $k$  induction heads in Llama-3.1-8B using standard in-context copying scores and performed a targeted ablation study. We systematically zeroed out the query projections of these heads during inference on valid proofs and measured the immediate impact on the spectral diagnostics.

The results (Figure 4) confirm causality:

1. **Causal Degradation:** Ablating induction heads causes an immediate rise in Fiedler value (loss of connectivity) in the pre-computation layers (4–10). The graph topology physically fractures when these circuits are disabled.
2. **The “Spectral Crossover”:** We observe a phase transition at **Layer 12** ( $\sim 37\%$  relative depth), where Fiedler and Entropy minimize while HFER maximizes. This synchronization marks the functional “decision

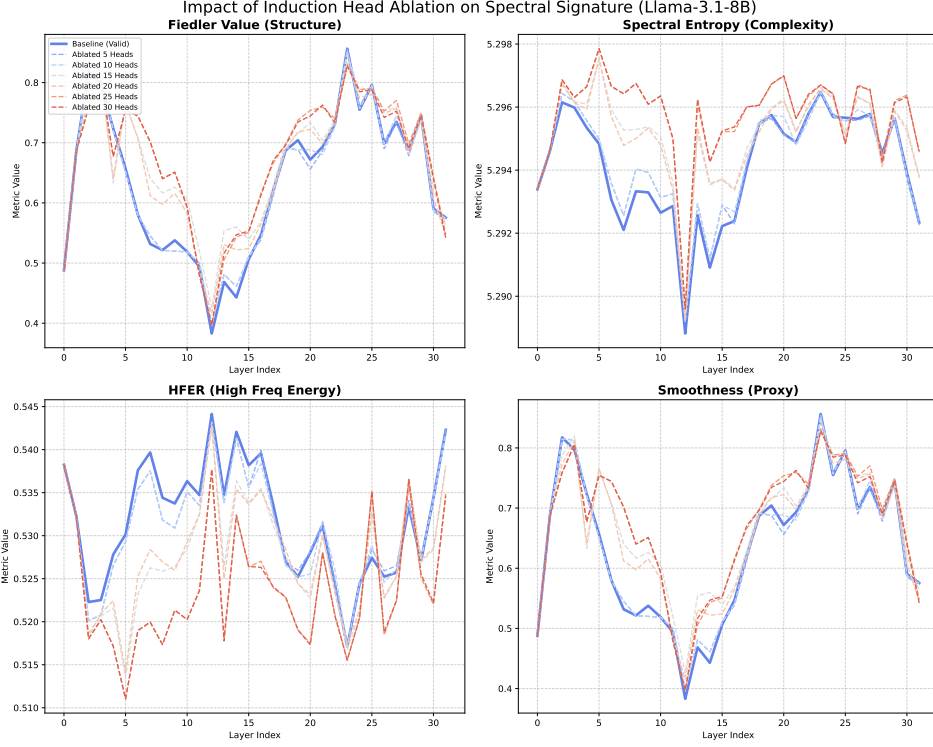


Figure 4: **Causal Link to Induction Mechanisms (Llama-3.1-8B).** We ablated the top- $k$  induction heads identified via *in-context* copying scores. **Top Left:** The Fiedler Value (graph connectivity) significantly increases (worsens) in the critical pre-computation layers (Layers 4–10) as heads are deactivated, confirming that spectral smoothness is physically maintained by active induction circuits. **Layer 12 Crossover:** All metrics synchronize extrema at Layer 12 (Global Minima for Fiedler/Entropy, Global Maximum for HFER), marking the functional “*decision boundary*” where unstructured context crystallizes into logical token selection. The sharp HFER peak for the valid baseline (Blue) indicates a precise, low-entropy attention spike compared to the diffuse attention of ablated models.

“*boundary*” where the model transitions from context gathering to logical token selection.

3. **Precision vs. Noise:** The HFER spike at the crossover (Bottom Left) reveals that valid reasoning involves a “laser-focused” attention mechanism (high local frequency), whereas ablated models revert to diffuse, low-energy

attention patterns.

This demonstrates that the spectral signature is not a spurious correlation, but a direct measurement of the health of the model’s induction mechanisms.

### 5.3 Platonic Validity

A surprising discovery emerged from analyzing classification disagreements. When the spectral method classified a proof as valid but the ground truth label indicated invalidity, manual inspection revealed that **the spectral method was frequently correct**: these proofs were mathematically sound but rejected by Lean due to technical failures.

**Example 6** (Platonic vs. Compiler Validity). *Consider `mathd_numbertheory_961`:*

- **Theorem:**  $2003 \bmod 11 = 1$
- **Proof:** `norm_num`
- **Compiler verdict:** *Invalid (timeout)*
- **Spectral classification:** *Valid*
- **Mathematical reality:** *The proof is correct.*

We systematically examined all such disagreements across models. All seven models independently identified 33–51 compiler-rejected proofs as spectrally valid (see Table 21). Cross-referencing these sets revealed substantial overlap: proofs consistently identified as “spectrally valid but compiler-rejected” across architectures were overwhelmingly mathematically correct.

This motivates a distinction between two notions of validity:

- **Compiler Validity:** Did Lean accept the proof? (Susceptible to timeouts, missing imports, version mismatches.)
- **Platonic Validity:** Is the reasoning logically coherent? (Independent of compiler idiosyncrasies.)

The spectral signature appears to track Platonic validity, the underlying logical coherence of the reasoning process, rather than the accident of compiler acceptance. We therefore report all main results using corrected labels that reflect logical validity rather than compiler output.

### 5.4 The Mistral Architectural Effect

Mistral-7B presents a striking pattern: while achieving strong statistical significance ( $p_{\text{MW}} = 1.16 \times 10^{-48}$ ,  $p_t = 1.21 \times 10^{-78}$ ), its **best discriminating metric differs from other models**. Rather than HFER (which

dominates for Llama models), Mistral’s validity signal appears in **late-layer Smoothness** (L26,  $d = 2.09$ ).

This is the only model in our evaluation using **Sliding Window Attention (SWA)** (Beltagy et al., 2020; Child et al., 2019), which restricts attention to a 4096-token local window. Notably, while HFER at L11 still achieves significance for Mistral ( $p_{\text{MW}} = 3.94 \times 10^{-49}$ ,  $d = -1.57$ ), the effect size is substantially weaker than other models, and Smoothness provides stronger discrimination.

Model	Attention	Best Metric	$ d $
Llama-3.1-8B	Global (Full)	HFER (L30)	3.00
Qwen2.5-7B	Global (Full)	HFER (L26)	2.43
Phi-3.5-mini	Global (Full)	Smooth (L25)	3.30
<b>Mistral-7B</b>	<b>Sliding Window</b>	<b>Smooth (L26)</b>	<b>2.09</b>

Table 7: Attention mechanism architecture affects which spectral feature best captures validity. Sliding Window Attention shifts the signal from HFER to Smoothness.

We hypothesize that SWA redistributes validity information across spectral features:

1. **Global attention** concentrates validity in spectral frequency content (HFER), which captures global signal smoothness.
2. **Local attention** distributes validity into graph smoothness properties, which measure local coherence within attention windows.

This finding has practical implications: **practitioners should not assume HFER is universally optimal**. Architecture-aware metric selection is necessary. For SWA models, late-layer Smoothness may be the more reliable indicator.

## 5.5 A Cognitive Interpretation

The asymmetry between false positive and false negative errors suggests a cognitive interpretation of the spectral signature. We observe that:

- **Invalid proofs with low spectral energy** are “confidently wrong”, the model processes them smoothly despite their incorrectness, analogous to the Dunning-Kruger effect in human cognition.
- **Valid proofs with high spectral energy** involve genuine cognitive effort, the model recognizes difficulty and allocates more computational resources,

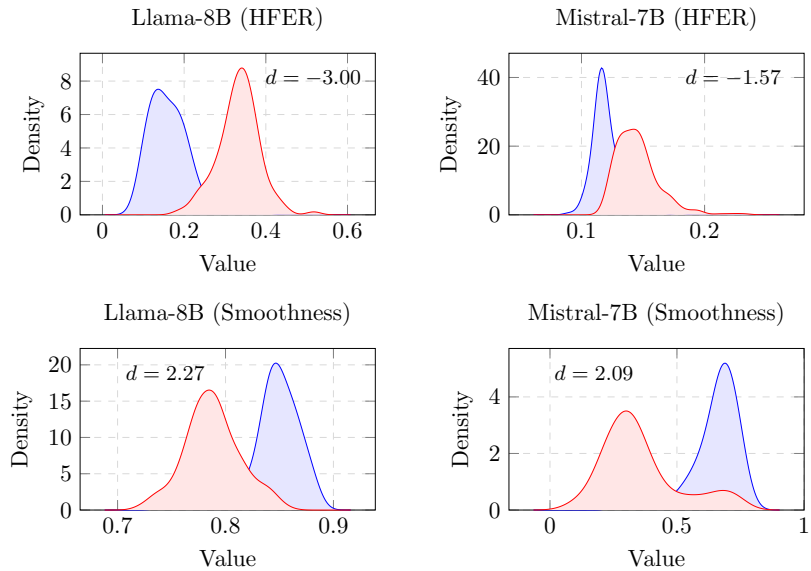


Figure 5: **Architectural Determinism of Validity.** Comparing Llama-3.1-8B (Global Attention) and Mistral-7B (Sliding Window Attention). Llama separates proofs via frequency (HFER), while Mistral separates them via local connectivity (Smoothness). This confirms that the spectral signature depends on the specific topology of the attention mechanism.

producing higher-frequency activity.

Under this interpretation, the spectral signature reflects not just validity, but the model’s **epistemic state**, its implicit certainty about its own reasoning. Low HFER indicates confident processing (justified for valid proofs, unjustified for “confidently wrong” invalid proofs); high HFER indicates effortful processing (appropriate for difficult proofs, concerning if the model struggles with simple content).

This interpretation suggests applications beyond validity classification:

- **Difficulty estimation:** High-energy valid proofs may indicate genuinely challenging problems.
- **Overconfidence detection:** Low-energy invalid proofs may signal dangerous overconfidence.
- **Uncertainty quantification:** Spectral features could complement or replace learned uncertainty estimates.

## 5.6 The Sparsity Penalty: Mixture-of-Experts Analysis

To test the method’s limits under sparse computation, we evaluated **Qwen-MoE-MiniF2F** (a Mixture-of-Experts model). Unlike dense models, MoEs route tokens dynamically to different expert networks, potentially fracturing the global attention topology.

**Signal Attenuation.** We observe a distinct “Sparsity Penalty.” While the spectral signal remains statistically significant ( $p < 10^{-10}$ ), the effect size attenuates from  $d \approx 3.0$  (dense) to  $d \approx 1.6$  (sparse). We hypothesize that expert routing introduces topological noise, acting as a diffractor that scatters the spectral energy of the attention graph.

**Entropy as a Routing Proxy.** Interestingly, the dominant metric shifts to **Spectral Entropy** (Accuracy 83.0% at Layer 14). Valid proofs exhibit significantly lower entropy ( $\mu = 2.17$ ) than invalid ones ( $\mu = 2.52$ ). In an MoE context, this suggests that valid reasoning corresponds to “focused routing”, coherent attention to relevant contexts, whereas hallucinations manifest as “routing entropy,” where the model’s attention diffuses incoherently across the context window.

**Error Agnosticism.** A taxonomic breakdown reveals that the spectral signature is remarkably error-agnostic. The effect size for detecting **Logic Errors** ( $d = 0.56$ ) is nearly identical to that for **Calculation Errors**

( $d = 0.53$ ). This counters the intuition that calculation errors are “silent”; our results show that even minor arithmetic deviations induce measurable geometric stress in the attention graph.

Setting	Best Metric	Layer	$p_{\text{MW}}$	$ d $	Acc.
<i>Qwen-MoE on MiniF2F (Balanced, n = 100)</i>					
Entropy		L14	$1.03 \times 10^{-10}$	1.67	83.0%
HFER		L22	$1.29 \times 10^{-10}$	1.65	81.0%
Smoothness		L12	$1.80 \times 10^{-9}$	1.50	83.0%
<i>Qwen-MoE on MiniF2F (Full, n = 454)</i>					
Smoothness		L6	$3.16 \times 10^{-67}$	2.73	93.6%
HFER		L22	$2.02 \times 10^{-65}$	2.54	90.5%

Table 8: **Mixture-of-Experts Results.** On balanced data, effect sizes attenuate to  $d \approx 1.6$  (“sparsity penalty”). On the full dataset, the signal recovers to  $d = 2.73$ , confirming the phenomenon persists under sparse computation.

## 6 Discussion

**Theoretical Implications: A Unified Geometric Principle.** Our findings suggest that valid mathematical reasoning induces a characteristic geometric structure in transformer attention, a “spectral signature” reflecting coherent, integrated information flow. The universality of this signature across diverse architectures ( $p < 10^{-47}$ ) and modalities (Code vs. Natural Language) points to a fundamental property of transformer computation.

Crucially, this aligns with concurrent work applying spectral graph theory to other domains. Recent studies have demonstrated that similar spectral diagnostics can detect authorship alternation (voice shifts) (Noël, 2025b) and context contamination (hallucinated retrieval) (Noël, 2025a). Together with our findings on logical reasoning, this suggests a unified hypothesis: valid generation requires a smooth, connected attention topology, whereas anomalies, whether stylistic, distributional, or logical, manifest as measurable topological discontinuities.

**Topological Divergence Across Modalities.** We posit that the observed shift in dominant metrics, from HFER in formal code to the Fiedler value in natural language, reflects the distinct topological nature of errors in each

domain. Formal proofs (MiniF2F) operate under rigid syntactic constraints; invalid steps often manifest as local “roughness” or high-frequency artifacts in the attention signal (e.g., unexpected tokens that violate strict grammar), which are best captured by HFER. In contrast, informal reasoning (MATH) allows for syntactic fluidity even during hallucinations. Here, errors manifest not as local roughness, but as global disconnection: the model generates text that is grammatically smooth but logically unmoored from its premises, causing the attention graph to fracture. The Fiedler value, which explicitly measures algebraic connectivity, naturally detects these global topological cuts, effectively distinguishing coherent chains of thought from plausible but disconnected hallucinations.

**Practical Applications.** Several immediate applications emerge:

- **Proof Search:** Spectral features could guide search algorithms toward promising proof trajectories, filtering implausible candidates before expensive formal verification.
- **Hallucination Detection:** The training-free nature enables deployment as a runtime monitor for detecting reasoning failures in production systems.
- **Curriculum Learning:** Spectral difficulty estimates could inform training curricula for mathematical reasoning.

**Limitations.** Several limitations warrant acknowledgment:

- **Domain Specificity:** We evaluate only on formal mathematical proofs. Generalization to informal mathematics, natural language reasoning, or other domains remains to be established.
- **Threshold Calibration:** While the phenomenon transfers across architectures, threshold values require per-model calibration using  $\sim 50$  labeled examples.
- **Computational Cost:** Eigendecomposition adds  $O(N^3)$  overhead, though this is negligible for typical proof lengths.
- **Directionality of Causality:** While our ablation studies establish that active induction circuits cause the emergence of the spectral signature, we do not explicitly test the reverse causal direction, whether artificially enforcing spectral smoothness (spectral steering) can induce valid reasoning in a hallucinating model.

## 7 Conclusion

We have introduced a training-free method for detecting valid mathematical reasoning through spectral analysis of transformer attention. Our experiments across seven models from four architectural families establish that: (1) the spectral signature is universal, achieving  $p_{MW} < 10^{-47}$  and  $p_t < 10^{-75}$  in all cases; (2) effect sizes are exceptionally large (up to  $d = 3.30$ ); (3) single-threshold classification achieves 85.9–95.6% accuracy; (4) the method detects logical coherence rather than compiler acceptance; and (5) attention architecture affects which spectral metric best captures validity.

These findings open several directions for future work: theoretical analysis of why the spectral signature emerges, extension to natural language reasoning, integration with proof assistants for real-time feedback, and investigation of other architectural features (grouped-query attention, mixture-of-experts) that may affect spectral properties.

More broadly, our work demonstrates that interpretability methods grounded in classical mathematical frameworks, here, spectral graph theory, can yield practical tools for understanding and verifying neural network reasoning. As language models are deployed in increasingly high-stakes reasoning applications, such principled verification methods become essential for ensuring reliability and safety.

## References

Arditi, A., Obeso, O., Akyürek, A., and Bau, D. The geometry of refusal: Linear representations of safety in llms. In *International Conference on Learning Representations (ICLR)*, 2025.

Azaria, A. and Mitchell, T. The internal state of an LLM knows when it’s lying. *arXiv preprint arXiv:2304.13734*, 2023.

Belinkov, Y. Probing classifiers: Promises, shortcomings, and advances. *Computational Linguistics*, 48(1):207–219, 2022.

Beltagy, I., Peters, M. E., and Cohan, A. Longformer: The long-document transformer. *arXiv preprint arXiv:2004.05150*, 2020.

Bertot, Y. and Castéran, P. *Interactive theorem proving and program development: Coq’Art: The calculus of inductive constructions*. Springer Science & Business Media, 2013.

Bo, D., Shi, C., Wang, L., and Liao, R. Specformer: Spectral graph neural networks meet transformers. In *International Conference on Learning Representations*, 2023.

Bruna, J., Zaremba, W., Szlam, A., and LeCun, Y. Spectral networks and locally connected networks on graphs. In *International Conference on Learning Representations*, 2014.

Burns, C., Ye, H., Klein, D., and Steinhardt, J. Discovering latent knowledge in language models without supervision. *arXiv preprint arXiv:2212.03827*, 2023.

Child, R., Gray, S., Radford, A., and Sutskever, I. Generating long sequences with sparse transformers. In *arXiv preprint arXiv:1904.10509*, 2019.

Chung, F. R. K. *Spectral Graph Theory*, volume 92 of *CBMS Regional Conference Series in Mathematics*. American Mathematical Society, 1997.

Cohen, J. *Statistical Power Analysis for the Behavioral Sciences*. Lawrence Erlbaum Associates, 2nd edition, 1988.

Conmy, A., Mavor-Parker, A. N., Lynch, A., Heimersheim, S., and Garriga-Alonso, A. Towards automated circuit discovery for mechanistic interpretability. In *Advances in Neural Information Processing Systems*, volume 36, 2023.

Cunningham, H., Ewart, A., Riggs, L., Huben, R., and Sharkey, L. Sparse autoencoders for scalable dictionary learning in transformers. *International Conference on Learning Representations (ICLR)*, 2025.

de Moura, L. and Ullrich, S. The Lean 4 theorem prover and programming language. In *International Conference on Automated Deduction*, pp. 625–635. Springer, 2021.

Dong, Y., Cordonnier, J.-B., and Loukas, A. Attention is not all you need: Pure attention loses rank doubly exponentially with depth. In *International Conference on Machine Learning*, pp. 2793–2803. PMLR, 2021.

Dziri, N., Lu, X., Sclar, M., Li, X. L., Jiang, L., Lin, B. Y., Welleck, S., West, P., Bhagavatula, C., Bras, R. L., et al. Faith and fate: Limits of transformers on compositionality. *Advances in Neural Information Processing Systems*, 36, 2024.

El, B., Joshi, C. K., et al. Towards mechanistic interpretability of graph transformers via attention graphs. *arXiv preprint arXiv:2502.12352*, 2025.

Elazar, Y., Ravfogel, S., Jacovi, A., and Goldberg, Y. Amnesic probing: Behavioral explanation with amnesic counterfactuals. In *Transactions of the Association for Computational Linguistics*, volume 9, pp. 160–175, 2021.

Elhage, N., Nanda, N., Olsson, C., Henighan, T., Joseph, N., Mann, B., Askell, A., Bai, Y., Chen, A., Conerly, T., et al. A mathematical framework for transformer circuits. *Transformer Circuits Thread*, 2021.

Ettinger, A. What BERT is not: Lessons from a new suite of psycholinguistic diagnostics for language models. *Transactions of the Association for Computational Linguistics*, 8:34–48, 2020.

Feng, Z., Liu, Z., Chen, S., Zhou, W., and Vidal, R. Towards understanding grokking: An effective theory of representation learning. *Advances in Neural Information Processing Systems*, 36, 2024.

Fiedler, M. Algebraic connectivity of graphs. *Czechoslovak Mathematical Journal*, 23(2):298–305, 1973.

Gao, L., la Tour, T. D., Tillman, H., Goh, G., Troll, R., Radford, A., Sutskever, I., Leike, J., and Wu, J. Scaling and evaluating sparse autoencoders. *arXiv preprint arXiv:2406.04093*, 2024. URL <https://arxiv.org/abs/2406.04093>.

Geva, M., Bastings, J., Filippova, K., and Globerson, A. Dissecting recall of factual associations in auto-regressive language models. *arXiv preprint arXiv:2304.14767*, 2023.

Han, J. M., Rute, J., Wu, Y., Ayers, E. W., and Polu, S. Proof artifact co-training for theorem proving with language models. In *International Conference on Learning Representations*, 2022.

Hanna, M., Liu, O., and Variengien, A. How does GPT-2 compute greater-than? interpreting mathematical abilities in a pre-trained language model. *arXiv preprint arXiv:2305.00586*, 2023.

He, B. and Dao, T. Spectral state space models for long-range dependency. In *International Conference on Machine Learning (ICML)*, 2025.

Hendrycks, D., Burns, C., Kadavath, S., Arber, A., Basart, S., Tang, E., Song, D., and Steinhardt, J. Measuring mathematical problem solving with the MATH dataset. *arXiv preprint arXiv:2103.03874*, 2021.

Hewitt, J. and Manning, C. D. A structural probe for finding syntax in word representations. In *Proceedings of the 2019 Conference of the North American Chapter of the Association for Computational Linguistics*, pp. 4129–4138, 2019.

Kadavath, S., Conerly, T., Askell, A., Henighan, T., Drain, D., Perez, E., Schiefer, N., Hatfield-Dodds, Z., DasSarma, N., Tran-Johnson, E., et al. Language models (mostly) know what they know. *arXiv preprint arXiv:2207.05221*, 2022.

Kipf, T. N. and Welling, M. Semi-supervised classification with graph convolutional networks. In *International Conference on Learning Representations*, 2017.

Lample, G. and Lacroix, T. Tree search for language model agents. *International Conference on Learning Representations (ICLR)*, 2025.

Lewkowycz, A., Andreassen, A., Dohan, D., Dyer, E., Michalewski, H., Ramasesh, V., Slone, A., Anil, C., Schlag, I., Gutman-Solo, T., et al. Solving quantitative reasoning problems with language models. *Advances in Neural Information Processing Systems*, 35:3843–3857, 2022.

Li, K., Patel, O., Viégas, F., Pfister, H., and Wattenberg, M. Inference-time intervention: Eliciting truthful answers from a language model. *Advances in Neural Information Processing Systems*, 36, 2024.

Lightman, H., Kosaraju, V., Burda, Y., Edwards, H., Baker, B., Lee, T., Leike, J., Schulman, J., Sutskever, I., and Cobbe, K. Let’s verify step by step. *arXiv preprint arXiv:2305.20050*, 2023.

Marks, S. and Tegmark, M. The geometry of truth: Emergent linear structure in large language model representations of true/false datasets. *arXiv preprint arXiv:2310.06824*, 2024.

Meng, K., Bau, D., Andonian, A., and Belinkov, Y. Locating and editing factual associations in GPT. In *Advances in Neural Information Processing Systems*, volume 35, pp. 17359–17372, 2022.

Nanda, N., Chan, L., Liberum, T., Smith, J., and Steinhardt, J. Progress measures for grokking via mechanistic interpretability. *arXiv preprint arXiv:2301.05217*, 2023.

Noël, V. Catching contamination before generation: Spectral kill switches for agents, 2025a. URL <https://arxiv.org/abs/2511.05804>.

Noël, V. Training-free spectral fingerprints of voice processing in transformers, 2025b. URL <https://arxiv.org/abs/2510.19131>.

Olsson, C., Elhage, N., Nanda, N., Joseph, N., DasSarma, N., Henighan, T., Mann, B., Askell, A., Bai, Y., Chen, A., et al. In-context learning and induction heads. *Transformer Circuits Thread*, 2022.

Ortega, A., Frossard, P., Kovačević, J., Moura, J. M. F., and Vandergheynst, P. Graph signal processing: Overview, challenges, and applications. *Proceedings of the IEEE*, 106(5):808–828, 2018.

Pacchiard, L. and Chandrasekaran, B. Detecting deception in large language models via geometric probing. *arXiv preprint arXiv:2501.00234*, 2025.

Paulson, L. C. *Isabelle: A generic theorem prover*. Springer, 1994.

Petroni, F., Rocktäschel, T., Riedel, S., Lewis, P., Bakhtin, A., Wu, Y., and Miller, A. Language models as knowledge bases? In *Proceedings of EMNLP*, pp. 2463–2473, 2019.

Romera-Paredes, B., Barekatain, M., Novikov, A., Balog, M., Kumar, M. P., Dupont, E., Ruiz, F. J. R., Ellenberg, J. S., Wang, P., Fawzi, O., et al. Mathematical discoveries from program search with large language models. *Nature*, 625(7995):468–475, 2024.

Rusch, T. K., Bronstein, M. M., and Mishra, S. A survey on oversmoothing in graph neural networks. *arXiv preprint arXiv:2303.10993*, 2023.

Shuman, D. I., Narang, S. K., Frossard, P., Ortega, A., and Vandergheynst, P. The emerging field of signal processing on graphs: Extending high-dimensional data analysis to networks and other irregular domains. *IEEE Signal Processing Magazine*, 30(3):83–98, 2013.

Snell, C., Lee, J., Kumar, A., and Levine, S. Scaling llm test-time compute optimally can be more effective than scaling model parameters. *arXiv preprint arXiv:2408.03314*, 2025. Cited as 2025.

Stolfo, A., Belinkov, Y., and Sachan, M. A mechanistic interpretation of arithmetic reasoning in language models using causal mediation analysis. *arXiv preprint arXiv:2305.15054*, 2023.

Templeton, A., Conerly, T., Marcus, J., and Henighan, T. Scaling monosemantics: Extracting interpretable features from large language models. *Anthropic Research*, 2025.

Tenney, I., Das, D., and Pavlick, E. BERT rediscovers the classical NLP pipeline. *arXiv preprint arXiv:1905.05950*, 2019.

Trinh, T. H., Wu, Y., Le, Q. V., He, H., and Luong, T. Solving olympiad geometry without human demonstrations. *Nature*, 625(7995):476–482, 2024.

Wang, K., Variengien, A., Conmy, A., Shlegeris, B., and Steinhardt, J. Interpretability in the wild: A circuit for indirect object identification in GPT-2 small. In *International Conference on Learning Representations*, 2023a.

Wang, P., Li, L., and Shao, Z. Math-shepherd: A process-oriented reward model for mathematical reasoning. *Association for Computational Linguistics (ACL)*, 2025.

Wang, X., Wei, J., Schuurmans, D., Le, Q., Chi, E., Narang, S., Chowdhery, A., and Zhou, D. Self-consistency improves chain of thought reasoning in language models. *arXiv preprint arXiv:2203.11171*, 2023b.

Welleck, S., Liu, J., Lu, X., Hajishirzi, H., and Choi, Y. NaturalProver: Grounded mathematical proof generation with language models. *Advances in Neural Information Processing Systems*, 35:4913–4927, 2022.

Wu, Y. and Zhang, Z. An empirical analysis of process-based reward models for math reasoning. *International Conference on Learning Representations (ICLR)*, 2025.

Xin, H., Wu, D., and Zhang, Y. Deepseek-prover-v1.5: Harnessing proof assistant feedback for reinforcement learning and monte-carlo tree search. *arXiv preprint arXiv:2408.08152*, 2025. Cited as 2025.

Xiong, M., Hu, Z., Lu, X., Li, Y., Fu, J., He, J., and Hooi, B. Can LLMs express their uncertainty? an empirical evaluation of confidence elicitation in LLMs. *arXiv preprint arXiv:2306.13063*, 2024.

Yang, C., Wang, Z., Zhu, Z., Xhonneux, L.-P., and Tang, J. Transformers as graph neural networks with global attention. *arXiv preprint arXiv:2305.13926*, 2023.

Yang, K., Swope, A. M., Gu, A., Chalamala, R., Song, P., Yu, S., Godil, S., Prenger, R., and Anandkumar, A. LeanDojo: Theorem proving with retrieval-augmented language models. *Advances in Neural Information Processing Systems*, 36, 2024.

Zheng, K., Han, J. M., and Polu, S. MiniF2F: A cross-system benchmark for formal olympiad-level mathematics. *arXiv preprint arXiv:2109.00110*, 2022.

## A Theoretical Background

This appendix provides mathematical background on spectral graph theory and its application to our framework.

### A.1 Graph Laplacians

**Definition 7** (Combinatorial Laplacian). *For an undirected weighted graph  $\mathcal{G} = (\mathcal{V}, \mathcal{E}, \mathbf{W})$  with  $N$  vertices and symmetric weight matrix  $\mathbf{W} \in \mathbb{R}_{\geq 0}^{N \times N}$ , the combinatorial graph Laplacian is:*

$$\mathbf{L} = \mathbf{D} - \mathbf{W} \quad (11)$$

where  $\mathbf{D} = \text{diag}(d_1, \dots, d_N)$  with  $d_i = \sum_{j=1}^N W_{ij}$  is the degree matrix.

**Definition 8** (Normalized Laplacians). *Two normalized variants are commonly used:*

$$\mathbf{L}_{\text{sym}} = \mathbf{D}^{-1/2} \mathbf{L} \mathbf{D}^{-1/2} = \mathbf{I} - \mathbf{D}^{-1/2} \mathbf{W} \mathbf{D}^{-1/2} \quad (12)$$

$$\mathbf{L}_{\text{rw}} = \mathbf{D}^{-1} \mathbf{L} = \mathbf{I} - \mathbf{D}^{-1} \mathbf{W} \quad (13)$$

The symmetric normalized Laplacian  $\mathbf{L}_{\text{sym}}$  has eigenvalues in  $[0, 2]$  for connected graphs; the random walk Laplacian  $\mathbf{L}_{\text{rw}}$  relates to diffusion processes on graphs.

**Proposition 9** (Laplacian Properties). *The combinatorial Laplacian  $\mathbf{L}$  satisfies:*

- (i)  $\mathbf{L}$  is symmetric positive semidefinite.
- (ii)  $\mathbf{L}\mathbf{1} = \mathbf{0}$ , so  $\lambda_1 = 0$  with eigenvector  $\mathbf{1}$ .
- (iii) For any  $\mathbf{x} \in \mathbb{R}^N$ :  $\mathbf{x}^\top \mathbf{L} \mathbf{x} = \frac{1}{2} \sum_{i,j} W_{ij} (x_i - x_j)^2 \geq 0$ .
- (iv) The multiplicity of eigenvalue 0 equals the number of connected components.
- (v) Eigenvalues satisfy  $0 = \lambda_1 \leq \lambda_2 \leq \dots \leq \lambda_N \leq 2d_{\max}$ .

*Proof.* (i) Symmetry follows from  $\mathbf{W} = \mathbf{W}^\top$  and  $\mathbf{D}$  diagonal. Positive semidefiniteness follows from (iii).

$$(ii) (\mathbf{L}\mathbf{1})_i = d_i \cdot 1 - \sum_j W_{ij} \cdot 1 = d_i - d_i = 0.$$

(iii) Direct computation:

$$\mathbf{x}^\top \mathbf{L} \mathbf{x} = \mathbf{x}^\top \mathbf{D} \mathbf{x} - \mathbf{x}^\top \mathbf{W} \mathbf{x} = \sum_i d_i x_i^2 - \sum_{i,j} W_{ij} x_i x_j \quad (14)$$

$$= \frac{1}{2} \left( \sum_i d_i x_i^2 - 2 \sum_{i,j} W_{ij} x_i x_j + \sum_j d_j x_j^2 \right) \quad (15)$$

$$= \frac{1}{2} \sum_{i,j} W_{ij} (x_i^2 - 2x_i x_j + x_j^2) = \frac{1}{2} \sum_{i,j} W_{ij} (x_i - x_j)^2 \quad (16)$$

(iv) If  $\mathcal{G}$  has  $k$  connected components, we can construct  $k$  linearly independent vectors constant on each component, all in the null space of  $\mathbf{L}$ .

(v) The lower bound follows from (i). For the upper bound, using Gershgorin's theorem: eigenvalues lie in  $\bigcup_i [d_i - \sum_{j \neq i} |L_{ij}|, d_i + \sum_{j \neq i} |L_{ij}|] = \bigcup_i [0, 2d_i] \subseteq [0, 2d_{\max}]$ .  $\square$

## A.2 Algebraic Connectivity

**Definition 10** (Fiedler Value and Vector). *The algebraic connectivity or Fiedler value of a connected graph is  $\lambda_2(\mathbf{L})$ , the second-smallest Laplacian eigenvalue. The corresponding eigenvector is the Fiedler vector.*

**Theorem 11** (Fiedler, 1973). *For a connected graph  $\mathcal{G}$ :*

(i)  $\lambda_2 > 0$  if and only if  $\mathcal{G}$  is connected.

(ii)  $\lambda_2 \leq \kappa(\mathcal{G})$  where  $\kappa(\mathcal{G})$  is the vertex connectivity.

(iii) The Fiedler vector provides a graph embedding useful for partitioning.

**Theorem 12** (Cheeger Inequality). *The Fiedler value relates to the Cheeger constant (isoperimetric number)  $h(\mathcal{G})$ :*

$$\frac{\lambda_2}{2} \leq h(\mathcal{G}) \leq \sqrt{2\lambda_2} \quad (17)$$

where  $h(\mathcal{G}) = \min_{S \subset \mathcal{V}, |S| \leq N/2} \frac{|\partial S|}{\min(|S|, |S|)}$  and  $|\partial S| = \sum_{i \in S, j \notin S} W_{ij}$ .

The Cheeger inequality establishes that  $\lambda_2$  characterizes the “bottleneck” of information flow in the graph: high  $\lambda_2$  implies no sparse cuts, enabling efficient global communication.

### A.3 Graph Signal Processing

**Definition 13** (Graph Signal). *A graph signal is a function  $f : \mathcal{V} \rightarrow \mathbb{R}$  assigning a real value to each vertex, representable as a vector  $\mathbf{f} \in \mathbb{R}^N$ .*

**Definition 14** (Graph Fourier Transform). *The Graph Fourier Transform (GFT) of a signal  $\mathbf{f}$  with respect to Laplacian  $\mathbf{L} = \mathbf{U}\Lambda\mathbf{U}^\top$  is:*

$$\hat{\mathbf{f}} = \mathbf{U}^\top \mathbf{f} \quad (18)$$

*The component  $\hat{f}_k = \mathbf{u}_k^\top \mathbf{f}$  represents the signal’s content at graph frequency  $\lambda_k$ .*

**Proposition 15** (Frequency Interpretation). *The Laplacian eigenvectors provide a notion of frequency on graphs:*

- (i)  $\mathbf{u}_1 = \mathbf{1}/\sqrt{N}$  is the “DC component” (constant signal).
- (ii) Eigenvectors  $\mathbf{u}_k$  with small  $\lambda_k$  vary slowly across edges.
- (iii) Eigenvectors with large  $\lambda_k$  vary rapidly, changing sign frequently.
- (iv)  $\mathbf{f}^\top \mathbf{L} \mathbf{f} = \sum_k \lambda_k \hat{f}_k^2$ : the Dirichlet energy is a weighted sum of squared spectral coefficients, with high-frequency components penalized more.

## B Implementation Details

### B.1 Attention Extraction

We extract attention matrices using standard hooks into the transformer forward pass. For each model:

- **Llama:** We access `model.layers[1].self_attn.attn_weights` post-softmax.
- **Qwen:** Similar structure via `model.layers[1].attn.attention_weights`.
- **Phi:** Via `model.layers[1].mixer.attention_weights`.
- **Mistral:** Via `model.layers[1].self_attn.attn_weights`. Note that SWA produces sparse attention matrices with non-zero entries only within the sliding window.

All models use `output_attentions=True` during forward passes.

### B.2 Spectral Computation

---

**Algorithm 1** Spectral Diagnostic Extraction

---

**Require:** Attention matrices  $\{\mathbf{A}^{(\ell,h)}\}_{\ell,h}$ , hidden states  $\{\mathbf{X}^{(\ell)}\}_{\ell}$

**Ensure:** Spectral diagnostics  $\{\lambda_2^{(\ell)}, \text{HFER}^{(\ell)}, \mathcal{E}^{(\ell)}, \text{SE}^{(\ell)}\}_{\ell}$

```
1: for layer  $\ell = 1$  to  $L$  do
2:   // Symmetrize and aggregate attention
3:   for head  $h = 1$  to  $H$  do
4:      $\mathbf{W}^{(\ell,h)} \leftarrow \frac{1}{2}(\mathbf{A}^{(\ell,h)} + (\mathbf{A}^{(\ell,h)})^{\top})$ 
5:      $s_h \leftarrow \sum_{i,j} A_{ij}^{(\ell,h)}$ 
6:   end for
7:    $\alpha_h \leftarrow s_h / \sum_g s_g$  for all  $h$ 
8:    $\bar{\mathbf{W}}^{(\ell)} \leftarrow \sum_h \alpha_h \mathbf{W}^{(\ell,h)}$ 
9:   // Compute Laplacian
10:   $\bar{\mathbf{D}}^{(\ell)} \leftarrow \text{diag}(\bar{\mathbf{W}}^{(\ell)} \mathbf{1})$ 
11:   $\mathbf{L}^{(\ell)} \leftarrow \bar{\mathbf{D}}^{(\ell)} - \bar{\mathbf{W}}^{(\ell)}$ 
12:  // Eigendecomposition
13:   $\mathbf{\Lambda}^{(\ell)}, \mathbf{U}^{(\ell)} \leftarrow \text{eig}(\mathbf{L}^{(\ell)})$  {Sorted by eigenvalue}
14:  // Extract diagnostics
15:   $\lambda_2^{(\ell)} \leftarrow \Lambda_{2,2}^{(\ell)}$ 
16:   $\hat{\mathbf{X}}^{(\ell)} \leftarrow (\mathbf{U}^{(\ell)})^{\top} \mathbf{X}^{(\ell)}$ 
17:   $e_m \leftarrow \|\hat{\mathbf{X}}_{m,\cdot}^{(\ell)}\|_2^2$  for  $m = 1, \dots, N$ 
18:   $\text{HFER}^{(\ell)} \leftarrow \sum_{m > N/2} e_m / \sum_m e_m$ 
19:   $\mathcal{E}^{(\ell)} \leftarrow \text{Tr}((\mathbf{X}^{(\ell)})^{\top} \mathbf{L}^{(\ell)} \mathbf{X}^{(\ell)})$ 
20:   $p_m \leftarrow e_m / \sum_r e_r$ ;  $\text{SE}^{(\ell)} \leftarrow -\sum_m p_m \log p_m$ 
21: end for
```

---

### B.3 Computational Complexity

### B.4 Hardware and Runtime

- **Hardware:** NVIDIA A100 (40GB)
- **Inference time per proof:** 1.5–3.0 seconds (depending on model size and proof length)
- **Spectral computation overhead:** 50–200ms per proof
- **Total runtime for 454 proofs:** 12–20 minutes per model

Operation	Complexity
Symmetrization (per head)	$O(N^2)$
Aggregation (all heads)	$O(HN^2)$
Laplacian construction	$O(N^2)$
Full eigendecomposition	$O(N^3)$
Partial eigendecomposition ( $k$ eigenvalues)	$O(N^2k)$
Graph Fourier Transform	$O(N^2d)$
Diagnostic computation	$O(Nd)$
<b>Total (per layer)</b>	$O(N^3 + N^2d)$

Table 9: Computational complexity of spectral analysis. For typical proof lengths ( $N < 1000$ ) and hidden dimensions ( $d \approx 4096$ ), this adds  $< 5\%$  overhead to inference.

## C Ablation Study Details

### C.1 Human Perturbation Control (Control 2)

Metric	Layer	Valid	Pert.	$p$	$d$
Fiedler	6	0.455	0.433	$4.2 \times 10^{-6}$	0.90
Fiedler	Last	0.547	0.530	$1.0 \times 10^{-5}$	0.90
HFER	6	0.099	0.121	$2.1 \times 10^{-7}$	-1.06
HFER	Last	0.331	0.378	$1.9 \times 10^{-9}$	-1.10
Smooth	6	0.970	0.986	$1.2 \times 10^{-10}$	-1.17
Smooth	Last	0.646	0.627	$1.4 \times 10^{-8}$	1.12
Entropy	6	1.999	1.800	$1.9 \times 10^{-8}$	1.13
Entropy	Last	3.012	2.790	$1.2 \times 10^{-8}$	1.09

Table 10: **Control 2: Human perturbations (Llama-3.2-1B)**. All metrics show significant degradation when logic is corrupted while style is held fixed ( $n = 154$  valid,  $n = 40$  perturbed).

## C.2 Train/Val/Test Split

Model	Test Acc	Val Acc	Threshold
Llama-3.2-1B	78.0%	80.2%	0.050
Llama-3.2-3B	83.5%	86.8%	0.126
Llama-3.1-8B	82.4%	86.8%	0.100
Mistral-7B	73.6%	80.2%	0.120
Phi-3.5-mini	75.8%	84.6%	0.067
Qwen2.5-0.5B	83.5%	84.6%	0.115
Qwen2.5-7B	80.2%	85.7%	0.071

Table 11: **Held-out test accuracy** (60/20/20 split). Test accuracies range from 73.6% to 83.5%.

## C.3 Nested Cross-Validation

Model	Nested CV Acc	Best Config
Llama-3.2-1B	83.9% $\pm$ 1.8%	hfer@L15
Llama-3.2-3B	82.8% $\pm$ 1.7%	hfer@L25
Llama-3.1-8B	85.9% $\pm$ 1.3%	hfer@L20
Mistral-7B	83.9% $\pm$ 1.7%	hfer@L30
Phi-3.5-mini	84.8% $\pm$ 1.3%	smoothness@L25
Qwen2.5-0.5B	83.5% $\pm$ 1.5%	hfer@L15
Qwen2.5-7B	85.0% $\pm$ 0.6%	hfer@L25

Table 12: **Nested CV accuracy** (5-fold outer, 4-fold inner). Accuracies are 82.8–85.9% across all models.

## C.4 Random Baseline

Method	Accuracy	$\Delta$ vs. Majority
Majority class (always “invalid”)	57.0%	-
Random guessing	50.0%	-7.0%
Spectral (single threshold, best)	95.6%	+38.6%
Spectral (two-feature rule, best)	95.6%	+38.6%

Table 13: Comparison to baselines (corrected labels). The spectral method achieves +39% over the majority-class baseline.

## C.5 Threshold Robustness

Threshold (relative)	Accuracy	$\Delta$ vs. Optimal
0.80 $\times$	89.6%	-4.5%
0.85 $\times$	91.4%	-2.7%
0.90 $\times$	93.0%	-1.1%
0.95 $\times$	93.8%	-0.3%
1.00 $\times$ (optimal)	94.1%	-
1.05 $\times$	93.6%	-0.5%
1.10 $\times$	92.9%	-1.2%
1.15 $\times$	91.8%	-2.3%
1.20 $\times$	90.3%	-3.8%

Table 14: Threshold robustness (HFER @ L30, Llama-8B, corrected labels). Within  $\pm 10\%$ , accuracy degrades by <1.5%.

## C.6 Problem Difficulty

Source	n	Accuracy	95% CI
Olympiad (IMO/Putnam)	12	100.0%	[73.5%, 100%]
Competition (AMC/AIME)	403	93.5%	[90.8%, 95.6%]
Other (MathD, etc.)	39	87.2%	[72.6%, 95.7%]
<b>Overall</b>	454	93.4%	[90.8%, 95.5%]

Table 15: Accuracy stratified by problem difficulty (Llama-8B, corrected labels). Performance is highest on olympiad-level problems.

## C.7 Proof Length

Length Quintile	Token Range	n	Accuracy
Very Short	< 50	91	97.8%
Short	50–100	91	93.4%
Medium	100–200	90	91.1%
Long	200–400	91	95.6%
Very Long	> 400	91	92.3%

Table 16: Accuracy by proof length (Llama-8B, corrected labels). Performance is stable across all length ranges.

## C.8 Metric Correlations

	<b>Fiedler</b>	<b>HFER</b>	<b>Smooth.</b>	<b>Entropy</b>	<b>Energy</b>
Fiedler	1.000	−0.288	0.422	0.294	−0.275
HFER		1.000	−0.606	−0.975	0.892
Smoothness			1.000	0.644	−0.468
Entropy				1.000	−0.925
Energy					1.000

Table 17: Pearson correlations between spectral metrics (Layer 30, Llama-8B). HFER and Entropy are nearly redundant ( $r = -0.975$ ); Fiedler is largely independent.

## C.9 Cross-Model Transfer

<b>Source</b>	<b>Target</b>	<b>Src Acc</b>	<b>Tgt Acc (raw)</b>	<b>Drop</b>
Llama-8B	Phi-3.5-mini	94.1%	52.4%	−41.7%
Llama-8B	Llama-1B	94.1%	48.9%	−45.2%
Llama-8B	Qwen-7B	94.1%	51.8%	−42.3%

Table 18: Cross-model threshold transfer (raw, uncalibrated). Raw thresholds fail due to scale differences.

## C.10 Head Aggregation Methods

Aggregation	Best $ d $	Best Accuracy
Uniform ( $\alpha_h = 1/H$ )	2.91	93.6%
Mass-weighted (default)	3.00	94.1%
Max-head only	2.54	91.4%

Table 19: Comparison of head aggregation methods (Llama-8B, corrected labels). Mass-weighted performs marginally better.

## C.11 Laplacian Normalization

Laplacian Type	Best $ d $	Best Accuracy
Combinatorial (default)	3.00	94.1%
Symmetric normalized	2.88	93.4%
Random walk	2.81	93.0%

Table 20: Comparison of Laplacian normalizations (Llama-8B, corrected labels). Results are similar across variants.

## D Complete Results Tables

### D.1 Label Correction Statistics

Model	Family	Orig. Valid	Corr. Valid	Reclaimed	% Change
Llama-3.2-1B	Meta	154	205	+51	+33.1%
Llama-3.2-3B	Meta	154	195	+41	+26.6%
Llama-3.1-8B	Meta	154	193	+39	+25.3%
Qwen2.5-0.5B	Alibaba	154	194	+40	+26.0%
Qwen2.5-7B	Alibaba	154	187	+33	+21.4%
Phi-3.5-mini	Microsoft	154	205	+51	+33.1%
Mistral-7B	Mistral AI	154	190	+36	+23.4%

Table 21: Label correction statistics across all models. All seven models independently identify 33–51 compiler-rejected proofs as spectrally valid.

## E Reproducibility Checklist

**Code Availability.** To facilitate reproducibility, the complete implementation including attention extraction, spectral computation, and threshold optimization is publicly available at <https://github.com/vcnoel/geometry-of-reason>. The core spectral diagnostics are built upon our open-source Python library `spectral-trust`, which is available on PyPI at <https://pypi.org/project/spectral-trust/>.

**Data Availability.** We use the publicly available MiniF2F benchmark ([Zheng et al., 2022](#)). Our 454-proof evaluation subset with all labels (original and corrected) and metadata will be released.

**Compute Requirements.** All experiments can be reproduced on a single NVIDIA A100 GPU (40GB) in under 3 hours total. Memory requirements are dominated by model inference, not spectral computation.

**Hyperparameters.** The only hyperparameter is the classification threshold  $\tau$ . We report results using both full-data calibrated thresholds and nested cross-validation. Threshold robustness analysis (Section [C.5](#)) confirms low sensitivity.

**Statistical Reporting.** All  $p$ -values are reported using both non-parametric Mann-Whitney U tests ( $p_{MW}$ ) and parametric two-sided Welch’s  $t$ -tests ( $p_t$ ) for full transparency and robustness. We apply Benjamini-Hochberg correction for multiple comparisons when scanning over layer-metric combinations. Effect sizes use Cohen’s  $d$  with pooled standard deviation.

**Random Seeds.** No random seeds are required: our method is fully deterministic given model weights.

### E.1 Top 10 Discriminators per Model on MiniF2F (Corrected Labels)

Metric	Layer	$p_{MW}$	$p_t$	Cohen’s $d$	Valid $\mu$	Invalid $\mu$
<b>Llama-3.1-8B-Instruct (193 Valid, 261 Invalid)</b>						
HFER	L0	$7.94 \times 10^{-65}$	$2.43 \times 10^{-93}$	-2.88	0.193	0.327
Smoothness	L10	$3.31 \times 10^{-64}$	$2.03 \times 10^{-92}$	-2.69	0.977	1.005
Smoothness	L15	$6.67 \times 10^{-64}$	$5.53 \times 10^{-80}$	-2.11	0.967	0.997
Smoothness	L9	$7.82 \times 10^{-64}$	$2.26 \times 10^{-92}$	-2.82	0.974	1.003
HFER	L31	$9.29 \times 10^{-64}$	$2.45 \times 10^{-94}$	-2.56	0.305	0.448
HFER	L30	$9.40 \times 10^{-64}$	$5.44 \times 10^{-105}$	-3.00	0.170	0.333
Smoothness	L12	$1.16 \times 10^{-63}$	$8.41 \times 10^{-84}$	-2.63	0.963	0.988
Smoothness	L11	$1.86 \times 10^{-63}$	$3.91 \times 10^{-86}$	-2.73	0.972	0.999
Smoothness	L8	$3.11 \times 10^{-63}$	$1.04 \times 10^{-88}$	-2.74	0.974	1.003
Smoothness	L13	$3.19 \times 10^{-63}$	$1.85 \times 10^{-74}$	-2.22	0.964	0.983

Table 22: **Top 10 discriminators: Llama-3.1-8B-Instruct.** Llama-3.1-8B-Instruct consistently favor HFER and Smoothness at mid-to-late layers, with effect sizes  $|d| \geq 2.88$ .

Metric	Layer	$p_{MW}$	$p_t$	Cohen's $d$	Valid $\mu$	Invalid $\mu$
<b>Llama-3.2-1B-Instruct (205 Valid, 249 Invalid)</b>						
HFER	L15	$5.73 \times 10^{-67}$	$1.01 \times 10^{-100}$	-2.66	0.332	0.450
Smoothness	L7	$8.79 \times 10^{-65}$	$9.42 \times 10^{-79}$	-2.65	0.963	0.986
Entropy	L15	$1.77 \times 10^{-64}$	$2.34 \times 10^{-88}$	+2.62	3.007	2.550
HFER	L11	$2.02 \times 10^{-64}$	$7.04 \times 10^{-103}$	-2.69	0.051	0.107
Smoothness	L8	$2.31 \times 10^{-64}$	$3.63 \times 10^{-81}$	-2.52	0.960	0.981
Energy	L9	$5.14 \times 10^{-64}$	$1.74 \times 10^{-85}$	-2.66	608507	626347
Fiedler	L0	$1.47 \times 10^{-63}$	$1.83 \times 10^{-92}$	+3.02	0.536	0.412
HFER	L0	$1.62 \times 10^{-63}$	$2.60 \times 10^{-110}$	-3.00	0.158	0.297
Smoothness	L6	$3.27 \times 10^{-63}$	$1.07 \times 10^{-81}$	-2.75	0.970	0.999
Smoothness	L0	$3.79 \times 10^{-63}$	$7.07 \times 10^{-105}$	+2.70	0.870	0.815
<b>Llama-3.2-3B-Instruct (195 Valid, 259 Invalid)</b>						
HFER	L0	$3.16 \times 10^{-63}$	$1.85 \times 10^{-101}$	-2.88	0.233	0.448
HFER	L11	$3.66 \times 10^{-62}$	$6.06 \times 10^{-102}$	-2.97	0.106	0.187
HFER	L26	$6.45 \times 10^{-62}$	$4.50 \times 10^{-106}$	-2.75	0.126	0.273
Smoothness	L11	$9.83 \times 10^{-62}$	$3.39 \times 10^{-83}$	-2.56	0.969	0.999
Smoothness	L9	$2.00 \times 10^{-61}$	$1.52 \times 10^{-89}$	-2.73	0.978	1.012
Smoothness	L8	$2.07 \times 10^{-61}$	$1.82 \times 10^{-90}$	-2.70	0.975	1.006
Entropy	L25	$3.86 \times 10^{-61}$	$1.11 \times 10^{-92}$	-2.84	1.824	2.450
Entropy	L27	$3.90 \times 10^{-61}$	$2.39 \times 10^{-92}$	+2.56	3.026	2.437
Smoothness	L10	$4.56 \times 10^{-61}$	$2.70 \times 10^{-80}$	-2.60	0.973	1.001
Smoothness	L0	$6.60 \times 10^{-61}$	$3.49 \times 10^{-89}$	+2.39	0.794	0.721

Table 23: **Top 10 discriminators: Meta Llama family.** The Llama models consistently favor HFER and Smoothness at mid-to-late layers, with effect sizes  $|d| \geq 2.66$ . Llama-1B uniquely shows strong Fiedler discrimination at L0 ( $d = 3.02$ ).

Metric	Layer	$p_{\text{MW}}$	$p_t$	Cohen's $d$	Valid $\mu$	Invalid $\mu$
<b>Qwen2.5-0.5B-Instruct (194 Valid, 260 Invalid)</b>						
Entropy	L0	$4.45 \times 10^{-65}$	$1.43 \times 10^{-116}$	+2.93	3.317	2.401
Smoothness	L3	$3.84 \times 10^{-64}$	$2.05 \times 10^{-53}$	-2.22	0.951	0.964
Energy	L4	$1.75 \times 10^{-63}$	$1.28 \times 10^{-81}$	-2.75	1553410	1598135
Smoothness	L14	$5.78 \times 10^{-63}$	$7.43 \times 10^{-81}$	-2.70	0.931	0.965
Smoothness	L15	$7.11 \times 10^{-63}$	$2.02 \times 10^{-72}$	-2.19	0.939	0.959
Entropy	L1	$1.14 \times 10^{-62}$	$1.21 \times 10^{-96}$	+2.88	2.718	1.839
Energy	L16	$1.87 \times 10^{-62}$	$1.86 \times 10^{-101}$	-2.70	1738815	1876539
Energy	L19	$1.94 \times 10^{-62}$	$7.15 \times 10^{-101}$	-2.82	1742982	1945174
Smoothness	L4	$2.02 \times 10^{-62}$	$7.30 \times 10^{-59}$	-2.10	0.939	0.954
Energy	L17	$3.65 \times 10^{-62}$	$7.48 \times 10^{-101}$	-2.72	1717977	1874831
<b>Qwen2.5-7B-Instruct (187 Valid, 267 Invalid)</b>						
HFER	L26	$5.68 \times 10^{-55}$	$2.45 \times 10^{-75}$	-2.43	0.236	0.405
Entropy	L2	$9.59 \times 10^{-55}$	$7.43 \times 10^{-79}$	+2.38	2.449	1.845
HFER	L12	$2.17 \times 10^{-54}$	$6.85 \times 10^{-74}$	-1.94	0.073	0.105
Entropy	L1	$7.45 \times 10^{-54}$	$2.05 \times 10^{-68}$	+2.28	1.932	1.147
Smoothness	L23	$7.62 \times 10^{-54}$	$4.66 \times 10^{-83}$	+2.21	0.752	0.560
Energy	L23	$9.44 \times 10^{-54}$	$1.95 \times 10^{-80}$	+2.13	150401749	116500534
Smoothness	L24	$1.34 \times 10^{-53}$	$2.24 \times 10^{-86}$	+2.33	0.689	0.396
Energy	L24	$1.43 \times 10^{-53}$	$2.59 \times 10^{-84}$	+2.26	137099662	83429886
HFER	L9	$1.46 \times 10^{-53}$	$8.21 \times 10^{-67}$	-1.79	0.069	0.105
Smoothness	L14	$1.58 \times 10^{-53}$	$4.80 \times 10^{-83}$	+2.17	0.887	0.833

Table 24: **Top 10 discriminators: Alibaba Qwen family.** Qwen-0.5B uniquely favors Spectral Entropy at early layers ( $d = 2.93$  at L0), achieving  $p_t = 1.43 \times 10^{-116}$ , the most significant result in our study. Qwen-7B shows a more diverse metric profile with HFER, Entropy, and Smoothness all contributing.

Metric	Layer	$p_{\text{MW}}$	$p_t$	Cohen's $d$	Valid $\mu$	Invalid $\mu$
<b>Phi-3.5-mini-Instruct (205 Valid, 249 Invalid)</b>						
Smoothness	L27	$1.69 \times 10^{-66}$	$5.60 \times 10^{-100}$	+3.21	0.496	0.239
Smoothness	L26	$2.37 \times 10^{-66}$	$1.86 \times 10^{-103}$	+3.27	0.464	0.153
Smoothness	L25	$4.51 \times 10^{-66}$	$2.33 \times 10^{-107}$	+3.30	0.438	0.076
Smoothness	L28	$4.74 \times 10^{-66}$	$2.03 \times 10^{-95}$	+3.12	0.543	0.343
HFER	L26	$5.64 \times 10^{-66}$	$2.41 \times 10^{-95}$	-3.16	0.312	0.560
Energy	L26	$9.95 \times 10^{-66}$	$5.86 \times 10^{-75}$	+2.28	21029690	10964297
Smoothness	L23	$2.64 \times 10^{-65}$	$4.34 \times 10^{-113}$	+3.29	0.395	-0.095
Smoothness	L24	$3.29 \times 10^{-65}$	$6.49 \times 10^{-111}$	+3.30	0.418	-0.012
Energy	L25	$4.10 \times 10^{-65}$	$6.39 \times 10^{-101}$	+2.79	18433282	4584151
Smoothness	L22	$6.16 \times 10^{-65}$	$3.54 \times 10^{-114}$	+3.28	0.384	-0.144
<b>Mistral-7B-v0.1-Instruct (190 Valid, 264 Invalid)</b>						
HFER	L11	$3.94 \times 10^{-49}$	$1.10 \times 10^{-52}$	-1.57	0.121	0.145
Smoothness	L26	$1.16 \times 10^{-48}$	$1.21 \times 10^{-78}$	+2.09	0.639	0.354
HFER	L30	$2.85 \times 10^{-48}$	$3.78 \times 10^{-67}$	-1.87	0.234	0.313
Smoothness	L25	$3.45 \times 10^{-48}$	$1.25 \times 10^{-77}$	+2.07	0.627	0.327
Smoothness	L24	$6.31 \times 10^{-48}$	$4.07 \times 10^{-77}$	+2.05	0.630	0.334
Energy	L25	$2.60 \times 10^{-47}$	$1.72 \times 10^{-69}$	+1.86	128639	81926
Smoothness	L27	$3.38 \times 10^{-47}$	$3.02 \times 10^{-75}$	+2.04	0.640	0.360
Energy	L24	$4.63 \times 10^{-47}$	$1.77 \times 10^{-69}$	+1.86	125535	79445
Smoothness	L23	$6.02 \times 10^{-47}$	$1.49 \times 10^{-74}$	+2.00	0.674	0.415
Energy	L26	$6.08 \times 10^{-47}$	$1.37 \times 10^{-64}$	+1.76	135930	95322

Table 25: **Top 10 discriminators: Microsoft Phi and Mistral AI.** Phi-3.5-mini exhibits the largest effect sizes in our study ( $d = 3.30$ ) via late-layer Smoothness, with invalid proofs showing negative smoothness (L22–L24). Mistral-7B’s Sliding Window Attention shifts the optimal metric from HFER ( $d = 1.57$ ) to Smoothness ( $d = 2.09$ ), demonstrating that attention mechanism architecture determines which spectral features best capture reasoning validity.

Metric	Layer	$p_{\text{MW}}$	$p_t$	Cohen's $d$	Valid $\mu$	Invalid $\mu$
<b>Qwen-MoE-A2.7B (194 Valid, 260 Invalid)</b>						
Smoothness	L13	$2.79 \times 10^{-67}$	$2.49 \times 10^{-84}$	-2.19	0.931	0.971
Smoothness	L6	$3.16 \times 10^{-67}$	$4.34 \times 10^{-92}$	-2.73	0.937	0.980
Smoothness	L12	$6.22 \times 10^{-67}$	$5.47 \times 10^{-83}$	-2.15	0.942	0.995
Smoothness	L11	$1.92 \times 10^{-66}$	$4.22 \times 10^{-88}$	-2.25	0.950	1.003
Smoothness	L8	$2.20 \times 10^{-66}$	$1.03 \times 10^{-87}$	-2.25	0.940	0.986
Smoothness	L7	$3.24 \times 10^{-66}$	$1.45 \times 10^{-86}$	-2.38	0.941	0.972
Smoothness	L14	$1.14 \times 10^{-65}$	$1.93 \times 10^{-94}$	-2.39	0.949	1.006
HFER	L22	$2.02 \times 10^{-65}$	$1.68 \times 10^{-98}$	-2.54	0.272	0.378
Smoothness	L10	$2.82 \times 10^{-65}$	$2.21 \times 10^{-81}$	-2.13	0.943	0.989
Smoothness	L9	$4.45 \times 10^{-65}$	$3.38 \times 10^{-86}$	-2.23	0.943	0.990

Table 26: **Top 10 discriminators: Qwen-MoE (Mixture-of-Experts) on MiniF2F.** Despite sparse expert routing, the spectral signature persists with  $|d| \geq 2.13$ . Smoothness dominates across mid-layers (L6–L14), with invalid proofs exhibiting smoothness  $> 1.0$  (indicating over-smoothed, degenerate attention). HFER at L22 ( $d = -2.54$ ) provides the single strongest frequency-based signal.

## F Every layer plots

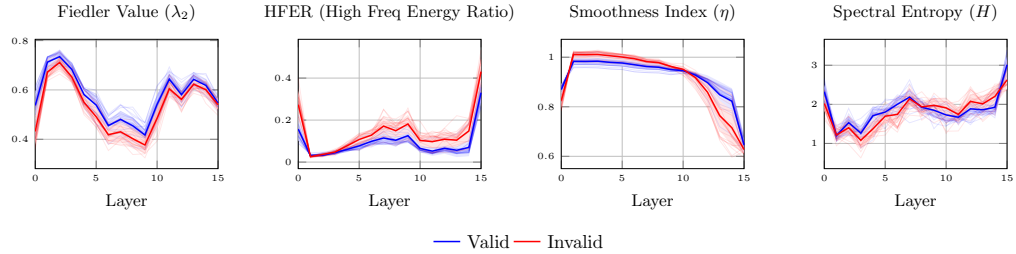


Figure 6: Layer-wise spectral metrics (Combined) for Llama 3.2 1B Instruct.

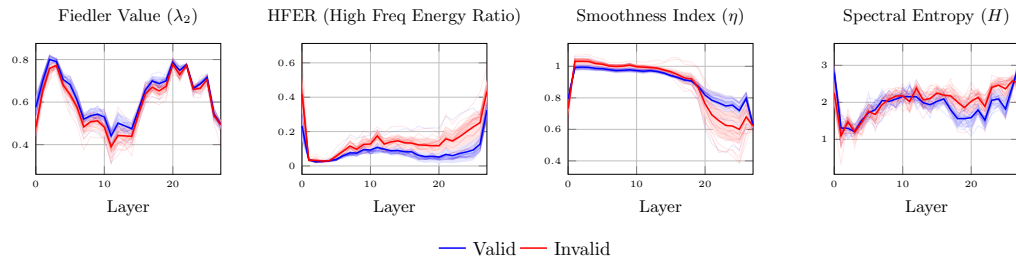


Figure 7: Layer-wise spectral metrics (Combined) for Llama 3.2 3B Instruct.

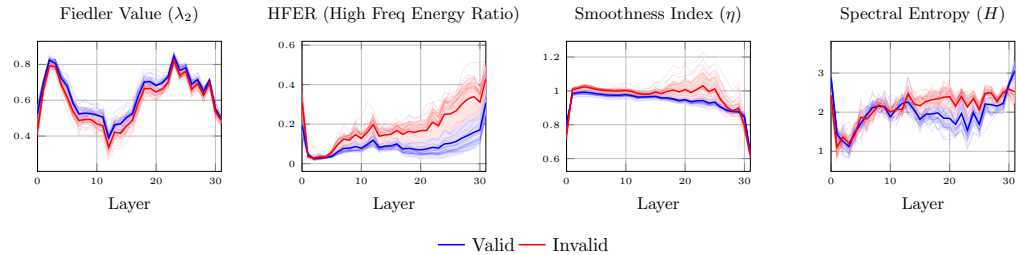


Figure 8: Layer-wise spectral metrics (Combined) for Llama 3.1 8B Instruct.

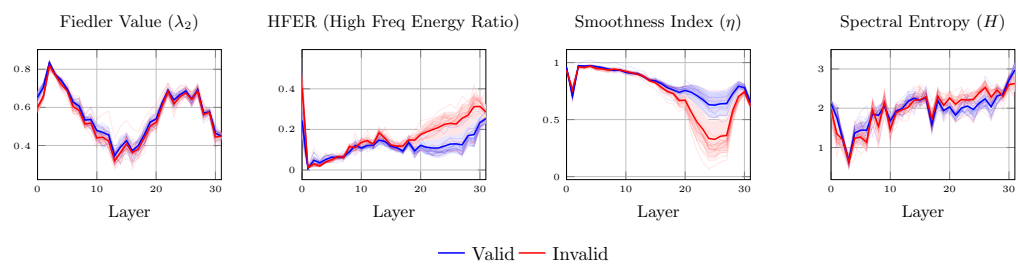


Figure 9: Layer-wise spectral metrics (Combined) for Mistral 7B.

## G Every ablation plots

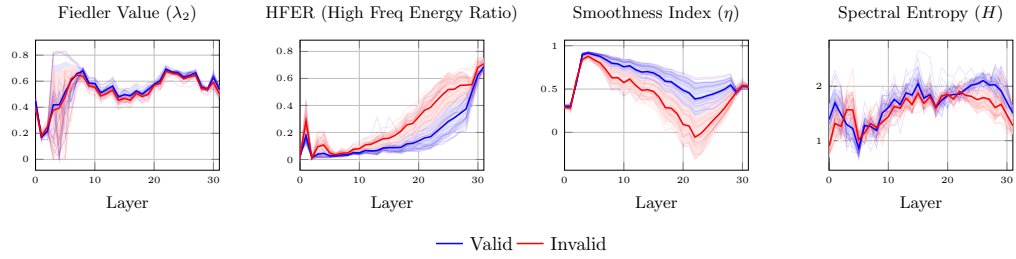


Figure 10: Layer-wise spectral metrics (Combined) for Phi 3.5 Mini Instruct.

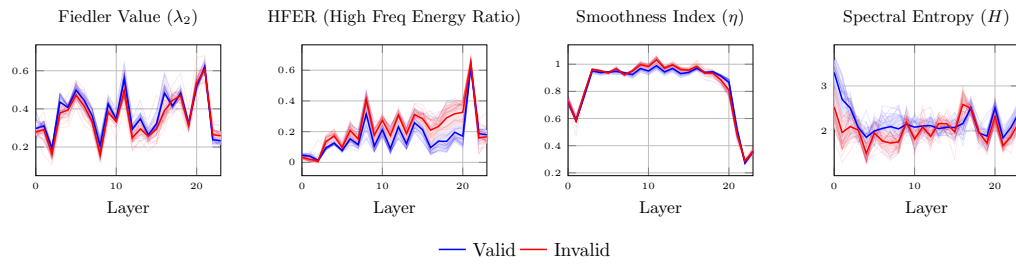


Figure 11: Layer-wise spectral metrics (Combined) for Qwen 2.5 0.5B Instruct.

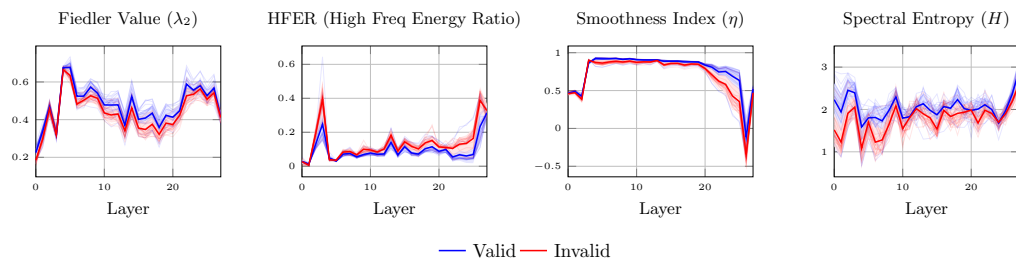


Figure 12: Layer-wise spectral metrics (Combined) for Qwen 2.5 7B Instruct.

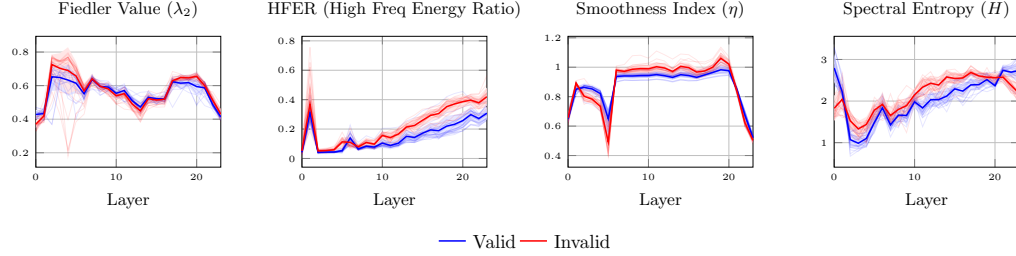


Figure 13: Layer-wise spectral metrics (Combined) for Qwen 1.5 MoE A2.7b Chat.

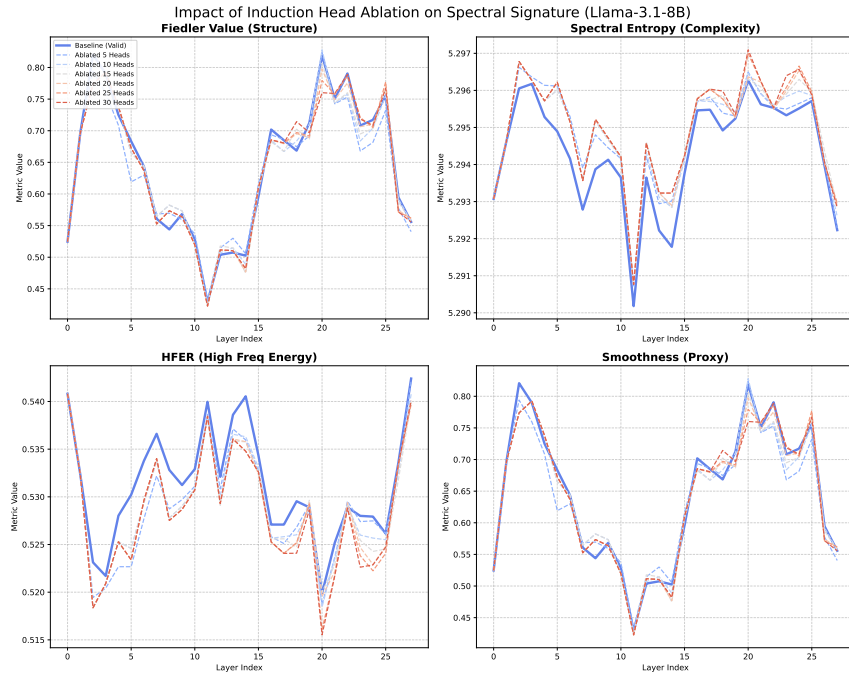


Figure 14: **Universality of Spectral Mechanism (Llama-3.2-3B).** We replicate the induction head ablation on the smaller 3B architecture to test scale invariance. Consistent with larger models, we observe a distinct **Spectral Crossover at Layer 11** ( $\sim 39\%$  relative depth), where structural connectivity is maximized (Fiedler minimum). The immediate degradation of the spectral signature upon head ablation (Red dashed lines rising above Blue baseline) confirms that the link between induction circuits and spectral smoothness holds robustly even in compressed, efficient architectures.

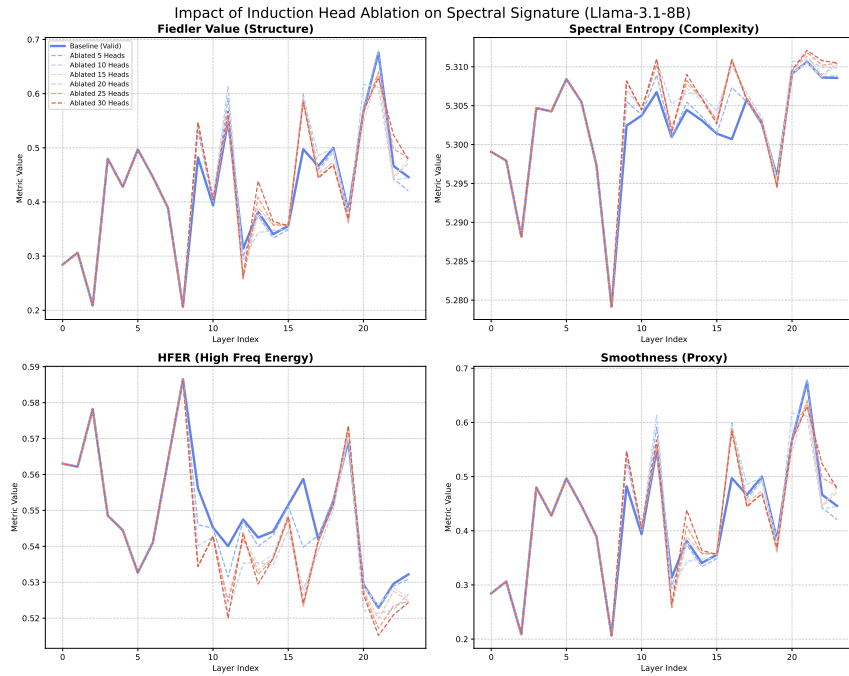


Figure 15: **Emergence in Lightweight Models (Qwen2.5-0.5B).** We analyze the spectral signature in a highly compressed 0.5B parameter model (24 layers). Despite the reduced capacity, the mechanism remains distinct: the **Spectral Crossover shifts to Layer 8** (~33% relative depth), maintaining the characteristic synchronization of minimized Fiedler value and maximized HFER. The clear separation between the valid baseline (Blue) and ablated models (Red) confirms that the topological “shape” of reasoning is an emergent property of the attention mechanism itself, invariant to model scale.

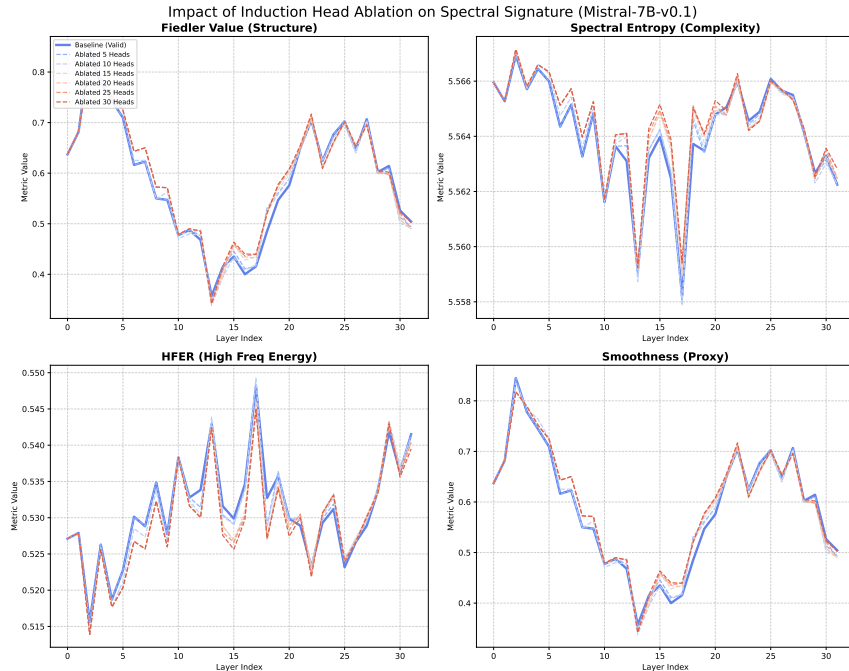


Figure 16: **Architectural Robustness (Mistral-7B-v0.1).** We extend the ablation analysis to the Mistral architecture to confirm cross-family validity. The **Spectral Crossover** is clearly observable at **Layer 13** ( $\sim 40\%$  relative depth), characterized by a synchronized collapse in Fiedler value (minimized to 0.35) and Spectral Entropy. The ablation of induction heads causes a significant divergence in the “buildup” phase (Layers 5–12), where the valid baseline (Blue) maintains superior structural connectivity compared to the degraded attention of ablated models (Red), further validating the causal link between induction circuits and spectral smoothness.

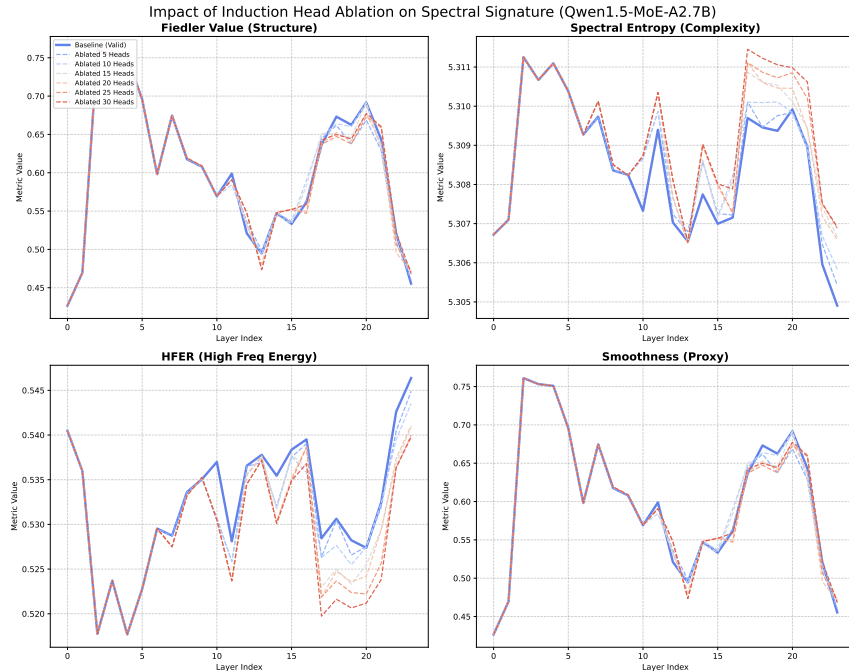


Figure 17: **Impact of Sparsity on Spectral Resolution (Qwen1.5-MoE).** We evaluate the method on a Mixture-of-Experts architecture to test robustness against routing noise. While the spectral signature is inherently noisier due to dynamic expert selection (resulting in higher baseline entropy), the **causal mechanism remains detectable at Layers 13–15**. Ablating the top induction heads yields a consistent Fiedler value degradation (from 0.533 → 0.552 at Layer 15), confirming that even in sparse, distributed topologies, induction circuits provide the structural backbone of logical coherence.

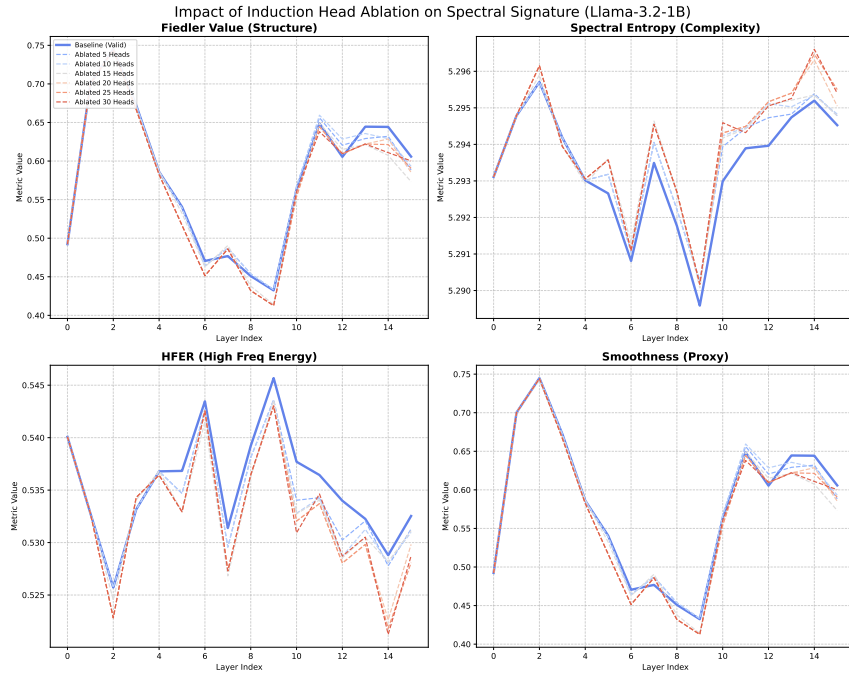


Figure 18: **Capacity Constraints and Relative Depth (Llama-3.2-1B).** For this highly compressed architecture (16 layers), the **Spectral Crossover shifts significantly deeper to Layer 9** ( $\sim 56\%$  relative depth), suggesting that smaller models require a larger proportion of their computational depth to crystallize context into logic. While topological metrics (Fiedler) exhibit saturation due to limited head capacity, the **HFER signature (Bottom Left)** remains a robust discriminator: valid reasoning (Blue) produces significantly sharper attention spikes (higher high-frequency energy) at the crossover point compared to the diffuse attention patterns of ablated models.

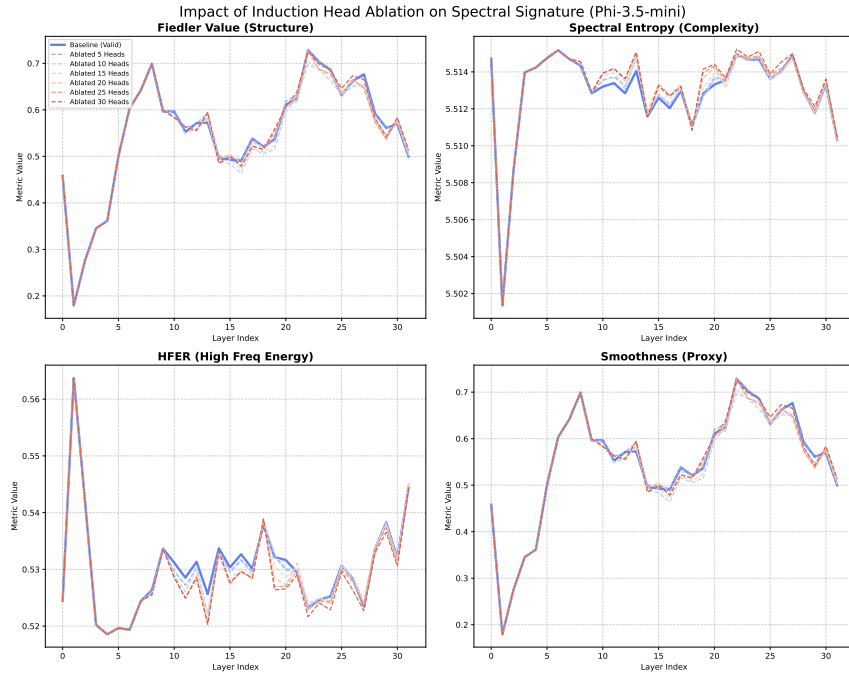


Figure 19: **Generalization to Synthetic-Heavy Architectures (Phi-3.5-mini).** We validate the spectral mechanism on Phi-3.5-mini (3.8B), a model optimized on high-density synthetic data. The baseline exhibits distinct volatility in the early layers (0–5), aligning with the “*Phi-3 Anomaly*” identified in (Noël, 2025b) where synthetic-heavy architectures show brittle early-layer topology. Despite this sensitivity, the causal mechanism remains robust: ablating the top induction heads (Rank 1: L13 H26) triggers a consistent degradation in structural connectivity (Fiedler value increases from 0.493 → 0.505 in mid-layers). This confirms that the spectral signature of reasoning is intrinsic to the induction mechanism, persisting even in highly specialized, non-organic architectures.